

Unravelling the Structure of Magnus' Pink Salt

Bryan E.G. Lucier,^a Karen E. Johnston,^a Wenqian Xu,^b
Jonathan C. Hanson,^b Sanjaya D. Senanayake,^b Siyu Yao,^c
Megan W. Bourassa,^d Monika Srebro,^{e,f} Jochen Autschbach,^{e,*}
and Robert W. Schurko^{a,*}

^a *Department of Chemistry and Biochemistry, University of Windsor,
Windsor, Ontario, Canada - N9B 3P4*

^b *Brookhaven National Laboratory, 2 Center Street, Upton, NY 11973, USA*

^c *Center for Computational Science & Engineering, and PKU Green Chemistry Centre,
Peking University, Beijing 100871, China*

^d *Department of Chemistry, Stony Brook University, Stony Brook, NY 11794, USA*

^e *Department of Chemistry, University at Buffalo, State University of New York, Buffalo, NY 14260-3000, USA*

^f *Department of Theoretical Chemistry, Faculty of Chemistry, Jagiellonian University
R. Ingardena 3, 30-060 Krakow, Poland*

* To whom correspondence should be addressed:

Phone: 519-253-3000 x3548, Fax: 519-973-7098, E-mail: rschurko@uwindsor.ca

Phone: 716-645-4122, Fax: 716-645-6963, Email: jochena@buffalo.edu

Abstract

A combination of multinuclear ultra-wideline solid-state NMR, powder X-ray diffraction, and X-ray absorption fine structure experiments, along with first principles calculations of platinum magnetic shielding tensors, have been employed to shed new light on the structures of Magnus' Green Salt (MGS) and Magnus' Pink Salt (MPS), $[\text{Pt}(\text{NH}_3)_4][\text{PtCl}_4]$, along with their synthetic precursors K_2PtCl_4 and $\text{Pt}(\text{NH}_3)_4\text{Cl}_2 \cdot \text{H}_2\text{O}$. A simple synthesis of MPS is detailed, which produces relatively pure product in good yield. Broad ^{195}Pt , ^{14}N , and ^{35}Cl SSNMR powder patterns have been acquired using the WURST-CPMG and BRAIN-CP/WCPMG pulse sequences. Experimentally measured and theoretically calculated platinum magnetic shielding tensors are shown to be very sensitive to not only the types and arrangements of coordinating ligands, but also to the intermolecular Pt-Pt metallophilic interactions. High-resolution ^{195}Pt NMR spectra of select regions of the broad ^{195}Pt powder patterns, in conjunction with an array of ^{14}N and ^{35}Cl spectra acquired using different pulse sequences and magnetic field strengths, reveal clear structural differences between the starting reagents, MGS and MPS, the latter of which has no known crystal structure to date. Powder X-ray diffraction patterns were acquired utilizing a synchrotron source; subsequent Rietveld refinements of this data were able to provide information on the space group and unit cell of MPS, as well as the positions of the Pt atoms. Analysis and fitting of X-ray absorption fine structure data provide an accurate measure of Pt-ligand bond lengths within MPS. A structural model for MPS is proposed, illustrating how the combination of ultra-wideline NMR, pXRD, and computational methods offers much promise for the future investigation and characterization of Pt-containing systems.

Introduction

The most commonly encountered structural motif for platinum in the 2+ oxidation state is the square planar complex. Square planar Pt(II) complexes are of great interest, both in terms of their synthesis and usage in many areas of chemistry¹⁻⁸ and biology.⁸⁻¹⁶ Much research has been devoted towards the development of optically active materials with “tunable” absorption and/or emission wavelengths, with practical applications in devices such as solid-state sensors, electronic switches or laser-based devices. In particular, systems that are based on a central square planar Pt(II) motif often exhibit unique optical properties, which are attributed to the metal-ligand interactions, Pt-Pt metallophilic interactions between adjacent layers, or both.^{5,17-21} The strength of the metallophilic interaction²²⁻²⁵ and concomitant optical/electronic activity often rely strongly on the Pt-Pt distance.

Two classic examples of colourful Pt complexes featuring metallophilic interactions are Magnus' salts, which have a long history of eluding structural characterization. Magnus' Green Salt (MGS), $[\text{Pt}(\text{NH}_3)_4][\text{PtCl}_4]$, is a highly insoluble “double-salt” initially reported by Magnus in 1828²⁶ and characterized as a one-dimensional polymeric complex of square planar Pt layers (Scheme 1) over one hundred years later in 1957.²⁷ The green colour of MGS is attributed to nearest-neighbor Pt-Pt metallophilic interactions between adjacent layers.^{28,29} For derivatives of MGS, a variety of colours, depending on temperature and coordinating ligands, is often observed, and thought to be the result of modification of the Pt-Pt distance between square planar layers.^{18,30,31} Interestingly, an elusive product known as Magnus' Pink Salt (MPS) may result during the synthesis of MGS under certain reaction conditions, although the isolation of a pure MPS product (without a MGS co-product) is very challenging.^{27,30,32,33} It is postulated that MPS exhibits only a faint pink colour

due to a longer Pt-Pt distance than that of MGS, and corresponding reduction in the strength of the Pt-Pt metallophilic interaction. Since MPS rapidly converts to MGS in solution, the growth of pure MPS crystals suitable for conclusive single-crystal X-ray diffraction (XRD) studies has proved elusive to date. The structure and composition of MPS are believed to be otherwise identical to MGS.²⁷

Structural characterization of such systems is challenging, particularly when XRD studies provide limited or no information (e.g., in cases of amorphous or partially disordered solids, or incident X-ray beam absorption by the compound, which sometimes arises in the study of Pt-based materials). The nature of the coordinating platinum environment determines the reactivity and stability of the complex; however, it is often difficult to probe this structural environment using conventional methods. Platinum-containing compounds are often characterized using optical spectroscopy, solution-state NMR (¹H, ¹³C and ¹⁹⁵Pt) and X-ray crystallography. ¹⁹⁵Pt solution-state NMR is widely employed,^{34,35} and has been studied extensively by theory.³⁶⁻³⁸ However, many platinum compounds have limited solubilities. In the case of highly soluble complexes, there is often only limited information available from ¹H and ¹³C NMR of organic ligands. Structural determination using XRD techniques are limited by (i) the ability to produce suitable single crystals and (ii) the crystallinity of the sample. In many cases, solid-state NMR (SSNMR) is ideal for structural characterization, as a complementary or standalone technique. In particular, SSNMR experiments on NMR-active transition metal nuclei, such as ¹⁹⁵Pt, can act as powerful structural probes for a wide array of materials.

The platinum NMR chemical shift (CS) is extremely sensitive to the local platinum environment, and has a known range of ca. 15 000 ppm.^{39,40} ¹⁹⁵Pt SSNMR powder patterns of square

planar platinum compounds yield information on the anisotropic chemical shift tensor and local electronic structure; however, they are often very broad and require time-consuming experiments to acquire. Conventional static and magic-angle spinning (MAS) ^{195}Pt NMR experiments often result in low signal-to-noise (S/N) ratios and spectra of poor quality. Experiments involving direct excitation (DE) of ^{195}Pt are often very lengthy, as ^{195}Pt T_1 values are usually on the order of tens of seconds to minutes in length. Cross-polarization (CP) experiments are an option, but are often ineffective. Under static conditions, the excitation bandwidths are extremely limited, and under the fast MAS conditions that are required for broad patterns, CP efficiency is greatly reduced. Furthermore, MAS experiments require that the magic angle be tuned with very high precision; even with accurate tuning, the low S/N and non-uniform distribution of signal over the manifold of spinning sidebands often yields unreliable CS tensor parameters.⁴¹

Recently, our research group introduced two pulse sequences that are effective for the efficient acquisition of ultra-wideline (UW) powder patterns. The Wideband Uniform-Rate Smooth-Truncation Carr-Purcell Meiboom-Gill (WURST-CPMG) pulse sequence⁴²⁻⁴⁶ is an echo-type sequence which employs WURST-80 pulses⁴⁵ for broadband excitation and a CPMG echo train for T_2 -dependent accumulation of echoes.⁴⁷ As an alternative to DE, if broadband CP is required, the Broadband Adiabatic Inversion pulses for Cross-Polarization (BRAIN-CP) pulse sequence may be applied.⁴⁸ BRAIN-CP features a rectangular pulse on the H-channel and a WURST-80 pulse on the X-channel, which serve to transfer polarization and store it along the $-z$ axis. A broadband conversion pulse is used to rotation polarization into the transverse plane. BRAIN-CP is easily combined with WURST-CPMG (the combination of the two has been termed BRAIN-CP/WCPMG). For brevity, WURST-CPMG and BRAIN-CP/WCPMG experiments are

referred to as DE and CP experiments, respectively. Both sequences are very useful for acquiring ^{195}Pt NMR spectra, and render many previously uninvestigated platinum-containing compounds as plausible targets for ^{195}Pt SSNMR characterization.^{41,49,50}

Herein, the use of multinuclear SSNMR experiments to study Magnus' salts and their associated starting reagents is discussed. ^{195}Pt SSNMR experiments conducted using the WURST-CPMG, BRAIN-CP/WCPMG, and conventional Hahn-echo pulse sequences reveal spectra which can be correlated to subtle structural differences between the two systems, via extraction of the platinum CS tensor parameters. ^{14}N and ^{35}Cl ultra-wideline SSNMR experiments are also utilized to probe the molecular structures and assess sample purity. Powder XRD experiments and concomitant Rietveld refinements and Le Bail fittings are utilized to predict a preliminary structure for MPS. Density functional theory (DFT) calculations of platinum nuclear magnetic shielding tensors, as well as an analysis of localized molecular orbitals which most influence shielding, lend insight into the relationships between NMR parameters and molecular structure. Finally, we propose a comprehensive structural model of MPS based on SSNMR, pXRD, and X-ray absorption fine structure (EXAFS) data, and discuss the use of these combined methodologies for the study of a wide array of Pt-containing systems.

Experimental

Sample Identities. $\text{Pt}(\text{NH}_3)_4\text{Cl}_2 \cdot \text{H}_2\text{O}$ [tetraamine platinum(II) chloride monohydrate], K_2PtCl_4 [potassium tetrachloroplatinate(II)], and $[\text{Pt}(\text{NH}_3)_4][\text{PtCl}_4]$ (Magnus' Green Salt, MGS) [tetraamine platinum(II) tetrachloroplatinate(II)] were purchased from Strem Chemicals, Inc. and used without further purification.

Synthesis of Magnus' Pink Salt (MPS). Syntheses of MPS were attempted utilizing previously reported procedures,^{18,27,30,51-53} however, we were unable to attain a reasonably pure, stable sample of MPS using these routes. Hence, a synthetic procedure was designed and optimized, which is detailed as follows: two individual 0.0026 M reagent solutions were prepared in separate flasks by dissolving either $\text{Pt}(\text{NH}_3)_4\text{Cl}_2 \cdot \text{H}_2\text{O}$ (30 mg) or K_2PtCl_4 (37 mg) in 3 mL H_2O , followed by the addition of 31 mL acetone while stirring. All solutions and glassware were cooled to near 0°C . Although acetone and water are generally miscible, the disparate volumes of water and acetone, low temperature of the system, and visual evidence of turbidity suggest that some degree of phase separation or containment (i.e., reverse micelles) was present. The individual reagent solutions were then stirred and subsequently combined. The resulting solution was stirred momentarily and then allowed to stand unagitated for ca. 10 s while a pink precipitate formed. The product was obtained as a pink powder via vacuum filtration of the reaction solution on a pre-chilled fine glass frit. The product was first washed with chilled acetone to remove any water from the sample via displacement and minimize MGS co-product formation. Following this, the product was washed with a minimal amount (< 10 mL) of chilled water to remove residual water-soluble reagents, $\text{Pt}(\text{NH}_3)_4\text{Cl}_2 \cdot \text{H}_2\text{O}$ and K_2PtCl_4 , followed by a final wash with chilled acetone. Once dry, the frit and product were heated at 120°C for at least two hours in a lab oven to remove any trace acetone and water. The product

was removed from the frit and its identity and purity were confirmed in a preliminary manner via known absorptions in its IR spectrum³⁰ (Supporting Information Table S1 and Supporting Information Figure S1) as well as elemental analysis (Table S2) and ¹H SSNMR (Table S3, Figure S2). The isolated yield of MPS was 70 %.

It is noted that after formation as a precipitate in solution, MPS rapidly converts to MGS if it is not removed from solution and dried. It takes ca. 6-12 hours for this conversion to occur to completion in the acetone/water volumes used in this synthesis. This transformation occurs much more rapidly at higher H₂O concentrations, particularly as the product dries on the frit. In addition, if the frit is moist when heated afterward, any MPS powder located on damp regions rapidly converts to MGS. Once isolated after heating, MPS is stable for at least six months (confirmed via SSNMR and IR analyses) under normal atmospheric conditions, but rapidly converts to MGS if exposed to bulk water or aqueous solution.

Solid-State NMR. All ¹H, ¹⁹⁵Pt and ¹⁴N solid-state NMR spectra were collected on a Varian Infinity Plus NMR spectrometer with an Oxford 9.4 T wide-bore magnet with $\nu_0(^1\text{H}) = 399.73$ MHz, $\nu_0(^{195}\text{Pt}) = 85.59$ MHz and $\nu_0(^{14}\text{N}) = 28.89$ MHz. All ¹H, ¹⁹⁵Pt, and ¹⁴N static (i.e., stationary sample) NMR experiments were conducted using a Varian/Chemagnetics 5 mm HX static probe. ¹⁹⁵Pt and ¹H magic-angle spinning (MAS) experiments were performed using a Varian/Chemagnetics 2.5 mm HX probe. All samples for static experiments were packed into 5 mm o.d. zirconia rotors or glass tubes, and samples for MAS experiments were packed into 2.5 mm o.d. zirconia rotors. A Chemagnetics low- γ tuning accessory and preamplifier were used on the X channel for all ¹⁴N NMR experiments. Platinum chemical shifts were referenced with respect to 1.0 M Na₂PtCl₆ (aq) ($\delta_{\text{iso}} = 0.0$ ppm) and nitrogen chemical shifts were reported with respect to NH₄Cl (s) ($\delta_{\text{iso}} = 0.0$ ppm).

All ultra-high field ^{35}Cl static NMR experiments were performed on a 21.1 T Bruker Avance II NMR spectrometer ($\nu_0(^{35}\text{Cl}) = 88.13$ MHz) at the National Ultrahigh-field NMR Facility for Solids in Ottawa, Ontario, Canada. Spectra were acquired on a home-built 4 mm HX probe, with samples packed into 4 mm o.d. glass NMR tubes. Chlorine chemical shifts were referenced to NaCl (s) ($\delta_{\text{iso}} = 0$ ppm). Detailed lists of parameters for all of the experiments discussed below are summarized in Tables S4-S12 of the Supporting Information.

^{195}Pt , ^{14}N and ^{35}Cl static UW NMR experiments were conducted using the WURST-CPMG pulse sequence.⁴²⁻⁴⁶ Since powder patterns are too broad to acquire in a single experiment, frequency-stepped acquisitions of individual sub-spectra were required, with the overall powder patterns constructed from the co-addition or skyline projection of sub-spectra.⁵⁴⁻⁵⁷ ^{195}Pt and ^{14}N NMR experiments used a 50 μs WURST-80 pulse, a sweep rate of 40 MHz/ms from high to low frequency over 2000 kHz, and a spectral width of 2000 kHz. ^{195}Pt and ^{14}N WURST-CPMG experiments used 200 and 110 points per echo, respectively, with experimentally optimized rf powers of 44 kHz and 30 kHz, respectively, and proton decoupling fields ranging from 24 to 37 kHz. For all ^{35}Cl WURST-CPMG NMR experiments, a spectral width of 1000 kHz and WURST sweep rate of 20 MHz/ms from high to low frequency were used, along with a ^{35}Cl rf power of 35 kHz and ^1H decoupling power of 20 kHz.

^1H - ^{14}N BRAIN-CP/WCPMG experiments⁴⁸ employed a Hartmann-Hahn matching field of 22 kHz, cross-polarization (CP) sweep rate of 40 kHz/ms across a total range of 400 kHz, refocusing WURST pulses across a range of 450 kHz, ^1H $\pi/2$ pulse widths of 4.00 μs , spectral widths of 2000 kHz, and ^1H decoupling fields of 25 kHz. The complete ^{14}N WURST-CPMG and BRAIN-CP/WCPMG NMR spectra were generated by mirroring the low-frequency (right) portion

of the powder pattern about $\delta = 0$ ppm, as described previously.^{41,58}

Static ¹⁹⁵Pt NMR spectra of discontinuity regions (vide infra) were acquired using a standard Hahn-echo experiment of the form $(\pi/2)_x - \tau_1 - (\pi)_y - \tau_2 - \text{acq}$, where τ_1 and τ_2 represent interpulse delays of 40 and 20 μs , respectively. A $\pi/2$ pulse width of 2.50 μs and spectral width of 2000 kHz were used, except for the low-frequency Hahn-echo experiment for MGS, where a $\pi/2$ pulse width of 6.63 μs and spectral width of 200 kHz were used. Corresponding ¹H-¹⁹⁵Pt static cross-polarization (CP) Hahn-echo NMR experiments employed ¹H $\pi/2$ pulse widths of 3.93 μs , a spectral width of 500 kHz, a Hartmann-Hahn matching field of 29 kHz, and a ¹H decoupling field of 37 kHz. ¹H-¹⁹⁵Pt BRAIN-CP/WURST-CPMG experiments⁴⁸ used a Hartmann-Hahn matching field of 29 kHz, CP sweep rate of 100 kHz/1 ms across a total range of 500 kHz, refocusing WURST pulse across a range of 2000 kHz, ¹H $\pi/2$ pulse widths of 3.93 μs , spectral widths of 2000 kHz, and ¹H decoupling field of 24 kHz. ¹⁹⁵Pt MAS NMR spectra of MGS were acquired using a standard Bloch-decay experiment, with a $\pi/2$ pulse width of 1.13 μs and spectral width of 1500 kHz. ¹H decoupling fields in excess of 70 kHz were applied for all MAS experiments.

¹H MAS NMR spectra were acquired at a spinning speed of 25 kHz using a standard Bloch decay pulse sequence, with a $\pi/2$ pulse width of 3.0 μs , spectral width of 200 kHz and recycle delay of 2 s.

Simulations of all static solid-state NMR spectra were performed using the WSOLIDS software package.⁵⁹ In all cases, uncertainties in extracted NMR tensor parameters for static spectra were estimated by visual inspection of best fit spectra and bidirectional variation in simulation parameters. Simulations of ¹⁹⁵Pt MAS NMR spectra were performed using the DMFit software program.⁶⁰

Theoretical Calculations. DFT computations of the platinum nuclear magnetic shielding (MS) tensors were performed with a developer's version of the Amsterdam Density Functional (ADF) package^{61,62} using the hybrid variant of the Perdew-Burke-Ernzerhof (PBE) functional,^{63,64} PBE0.^{65,66} A relativistic all-electron triple- ζ singly polarized (TZP) basis set from the ADF basis set library was employed for all atoms, except Pt for which the more flexible quadruple- ζ quadruply polarized (QZ4P) basis was used. As previous studies have shown, this basis set combination is well suited for efficient and reasonably accurate computations of Pt magnetic shielding tensors.^{36,67-69} Relativistic effects were incorporated in the computations by means of the Zeroth-Order Regular Approximation (ZORA).⁷⁰⁻⁷² In the numerical integration method used for the calculations, the general accuracy parameter was set to 4.0, while for the atomic core regions the accuracy parameter was set to 5.0. A criterion of 10^{-4} au was applied to remove linearly dependent basis function combinations. Natural Bond Orbital (NBO) and Natural Localized Molecular Orbital (NLMO) analyses were applied for the MS tensors.^{73,74} Details of the technique and a brief description of the sequence of calculations are discussed elsewhere.^{68,75} To ensure that all basis set functions were used in the analysis, the linear dependency criterion was decreased to 10^{-5} au. Symmetry was not explicitly utilized in the calculations.

The systems studied include model clusters of MGS, $\text{Pt}(\text{NH}_3)_4\text{Cl}_2 \cdot \text{H}_2\text{O}$ and K_2PtCl_4 . MPS was excluded from the theoretical analysis, since all of our attempts to obtain an adequately converged ground-state, as well as MS parameters close to experimental values, failed for this system. MS parameters were calculated from clusters extracted from experimental and/or optimized solid-state geometries (vide infra) to ensure the surroundings of the central Pt unit(s) were as close to the crystal environment as possible. Geometry optimizations of the atomic positions were

performed with periodic boundary conditions, using experimental lattice constants.^{27,76,77} The optimizations utilized the Plane-Wave Self-Consistent Field (PWscf) package,⁷⁸ version 4.2.1 from the Quantum-ESPRESSO suite of programs.⁷⁹ In the PWscf calculations the PBE functional was employed in conjunction with ultrasoft pseudopotentials (USPPs)⁸⁰ and plane-wave (PW) basis sets for the valence orbitals. The core levels and radii (in au) were [He](1.3), [He](1.4), [Ne](1.5), [Ar](1.6), and [Xe + 4f](1.8) for N, O, Cl, K, and Pt, respectively. For H, an “all-electron pseudopotential” was generated with a core radius of 0.9 au. The kinetic-energy cutoff for the PW basis sets was set to 40 Ry. A k -point sampling of $3 \times 3 \times 5$ for MGS and $4 \times 4 \times 7$ for reagents was used. In the case of MGS, stricter than default geometry convergence criteria were applied to match the experimental structure.

The geometry optimizations were successful in closely reproducing the experimental geometric parameters for MGS and K_2PtCl_4 . In the case of $\text{Pt}(\text{NH}_3)_4\text{Cl}_2 \cdot \text{H}_2\text{O}$, the calculated Pt-N distances are much smaller than those determined from an X-ray crystal structure.⁷⁶ The latter, more than 2.6 Å, seem to be unreasonably large, given typical Pt-N distances in square planar Pt moieties such as Benton's salt, $\text{Pt}(\text{NH}_3)_4\text{CuCl}_4$, (2.04 Å)⁸¹ or MGS (2.08 Å). We consider the calculated Pt-N distance of $\text{Pt}(\text{NH}_3)_4\text{Cl}_2 \cdot \text{H}_2\text{O}$ more reliable than the experimental estimate (vide infra).

Powder X-ray Diffraction. Room temperature powder X-ray diffraction (pXRD) experiments were completed at beamline X7B at the National Synchrotron Light Source (NSLS) of Brookhaven National Lab (BNL). Powdered samples were loaded into 0.5 ID Kapton capillaries. A Perkin-Elmer amorphous silicon area detector was used to collect XRD images in transmission mode. Rietveld refinements⁸² and Le Bail fittings were attempted on MGS and MPS using GSAS software.^{83,84} Fit2D was used to integrate two-dimensional data to one dimension,⁸⁵ and the

differential Fourier map of electron density was generated using FOX.⁸⁶

X-ray Absorption Fine Structure. X-ray Absorption Near Edge Spectroscopy (XANES) and Extended X-ray Absorption Fine Structure (EXAFS) measurements of the Pt complexes were collected at beamline X19A of the NSLS at BNL using a Si (111) monochromator (2×10^{-4} ($\Delta E/E$)). All the measurements were collected under transmission mode with an optimized ion chamber at the Pt L_{III} edge (11564 eV). The Pt salts were diluted to 20 % wt using fine BN powder and pressed to make 2 mm thick pellets for measurements. XANES and EXAFS spectra of the samples were analyzed using the Athena and Artemis programs employing the Feff 6.0 package

Elemental Analysis. Microanalyses were performed using a Perkin-Elmer 2400 Series II C, H, N analyzer in the Centre for Catalysis and Materials Research at the University of Windsor.

Infrared Spectroscopy. Fourier-transform infrared (FTIR) spectra were acquired using a Nicolet Magna 860 FTIR spectrometer coupled to a Continuum IR microscope (Thermo-Nicolet, Madison, WI) at beamline U2B in the NSLS. The microscope was equipped with a 32x Schwarzschild objective and a liquid nitrogen cooled mercury cadmium telluride detector. A thin layer of each sample was placed on a 1 mm thick calcium fluoride slide, and point spectra were acquired with a 50 μm aperture in transmission mode. For each spectrum, 64 scans were co-added with a 4 cm^{-1} spectral resolution over the mid-infrared region (1000-4000 cm^{-1}).

Results and Discussion

To begin, NMR spectra acquired with the ^{195}Pt WURST-CPMG and ^1H - ^{195}Pt BRAIN-CP/WCPMG pulse sequences are presented and discussed. High-resolution ^{195}Pt Hahn-echo and ^1H - ^{195}Pt CP-echo spectra of key diagnostic spectral regions are then presented, followed by ^{195}Pt MAS NMR spectra. ^{14}N WURST-CPMG and ^1H - ^{14}N BRAIN-CP/WCPMG experiments yield spectra which shed additional light on intermolecular interactions. Then, ^{35}Cl WURST-CPMG spectra of all systems are compared and contrasted, and related to differences in structure and symmetry. Powder XRD patterns and corresponding refinements, which were used to differentiate the compounds and conduct a structural analysis of MPS, are then discussed in detail. Following this, a brief discussion of EXAFS and XANES experimental data is included. A proposed structural model of MPS is presented from a combination of SSNMR, XRD, and EXAFS data. Finally, first principles calculations of platinum nuclear magnetic shielding (NMR) tensors for several model systems are compared with the experimentally derived data and interpreted in terms of NBO and LMO models of local bond and lone-pair contributions.

^{195}Pt WURST-CPMG experiments. ^{195}Pt NMR spectra of $\text{Pt}(\text{NH}_3)_4\text{Cl}_2\cdot\text{H}_2\text{O}$, K_2PtCl_4 , and MGS are shown in Figure 1(a) and 1(b), with corresponding CS tensor parameters found in Table 1. The K_2PtCl_4 spectrum was previously discussed in a separate work.⁵⁰ The ^{195}Pt powder patterns are indicative of single platinum sites each possessing axially symmetric CS tensors with $\kappa \approx -1$ (i.e., δ_{11} is the distinct component and $\delta_{22} \approx \delta_{33}$); axially symmetric tensors of this sort are commonly observed in square planar Pt(II) structural motifs.^{39,41,49,87-90} These powder patterns range across impressive breadths, with Ω values of 7250 ppm (640 kHz at 9.4 T) for $\text{Pt}(\text{NH}_3)_4\text{Cl}_2\cdot\text{H}_2\text{O}$ and 10420 ppm (920 kHz at 9.4 T) for K_2PtCl_4 . Despite this, the use of frequency-stepped acquisition and the

WURST-CPMG pulse sequence results in relatively short experimental times for both reagents (Table S4). There is a shorter recycle delay associated with $\text{Pt}(\text{NH}_3)_4\text{Cl}_2 \cdot \text{H}_2\text{O}$ due to its shorter $T_1(^{195}\text{Pt})$, which likely results from contributions to the longitudinal relaxation from ^{195}Pt - ^1H dipolar couplings (from both NH_3 and mobile H_2O) which are absent in K_2PtCl_4 .

At first glance, the spectrum of MGS (Figure 1(c)) appears to be composed of a simple superimposition of powder patterns corresponding to the individual reagents; however, the extracted CS tensors indicate otherwise. Simulations of the overall MGS powder pattern reveal that its $[\text{Pt}(\text{NH}_3)_4]^{2+}$ and $[\text{PtCl}_4]^{2-}$ units have ^{195}Pt CS tensors with significantly larger Ω and higher δ_{iso} values than those of the starting reagents. It is also noted that the Pt-Pt interlayer distances in $\text{Pt}(\text{NH}_3)_4\text{Cl}_2 \cdot \text{H}_2\text{O}$ and K_2PtCl_4 are 4.220 Å and 4.144 Å, respectively,^{76,77} but only 3.245 Å in MGS, inviting the preliminary hypothesis that the ^{195}Pt CS tensor is sensitive to Pt-Pt metallophilic interactions. These interactions occur perpendicular to the square plane, corresponding to the orientation of the δ_{11} component of the ^{195}Pt CS tensor (as predicted from molecular symmetry and the value of κ). Furthermore, δ_{11} is the only component that substantially differs between MGS and the starting reagents. In addition, we also note that the spectra associated with $[\text{Pt}(\text{NH}_3)_4]^{2+}$ and $[\text{PtCl}_4]^{2-}$ units in MGS are associated with distinct optimized ^{195}Pt NMR recycle delays, implying that each of the two unique Pt atoms has a disparate $T_1(^{195}\text{Pt})$ value. This mirrors the difference in recycle delays observed in the individual starting reagents (Table S4).

Attempts were made to study MPS via WURST-CPMG using the same experimental parameters utilized in the acquisition of spectra of MGS; however, these experiments resulted in a broad powder pattern of irregular shape (Figure S3). The long relaxation delays (40 s) employed in these experiments imply that the $T_1(^{195}\text{Pt})$ value for the $[\text{PtCl}_4]^{2-}$ unit in MPS is much longer than

those of similar Pt sites in MGS and K_2PtCl_4 . Since much longer relaxation delays render ^{195}Pt WURST-CPMG experiments impractical, the use of a CP experiment which relies on the much lower $T_1(^1\text{H})$ value would be advantageous (vide infra).

^1H - ^{195}Pt BRAIN-CP/WCPMG experiments. The recently-introduced BRAIN-CP pulse sequence,⁴⁸ which is readily combined with WURST-CPMG (BRAIN-CP/WCPMG), was utilized to acquire the ^{195}Pt powder pattern of MPS. These experiments offer potential S/N enhancement similar to CP, a broadband excitation similar to WURST-CPMG experiments, and a reliance on the generally shorter T_1 of the abundant nucleus (i.e., $T_1(^1\text{H}) < T_1(^{195}\text{Pt})$ in most cases). The ^{195}Pt NMR spectrum of MPS obtained using a ^1H - ^{195}Pt static BRAIN-CP/WCPMG experiment (Figure 1(d)) appears to be composed of two distinct patterns, presumably corresponding to $[\text{PtCl}_4]^{2-}$ and $[\text{Pt}(\text{NH}_3)_4]^{2+}$ ions. It is important to note that the $[\text{PtCl}_4]^{2-}$ species is detected in this spectrum, confirming the presence of strong dipolar couplings between the ^{195}Pt nuclei in $[\text{PtCl}_4]^{2-}$ units and the amine protons of $[\text{Pt}(\text{NH}_3)_4]^{2+}$ units. This infers that these species are proximate and are incorporated into the unique MPS compound (i.e., this sample is clearly not just a simple heterogeneous mixture of the two starting reagents). Analogous BRAIN-CP/WCPMG experiments on MGS and $\text{Pt}(\text{NH}_3)_4\text{Cl}_2 \cdot \text{H}_2\text{O}$ (Figure 1(e), (f)) require much shorter experimental times to obtain comparable S/N and higher resolution (Table S7).

The CS tensor parameters extracted from the ^{195}Pt powder pattern of MPS (Table 1) are almost identical to those of the corresponding K_2PtCl_4 and $\text{Pt}(\text{NH}_3)_4\text{Cl}_2 \cdot \text{H}_2\text{O}$ reagents. In other words, although CP experiments confirm that these units are spatially proximate within MPS, Pt-Pt metallophilic interactions are not present. This suggests a longer Pt-Pt distance in MPS in comparison to MGS. Interestingly, the low-frequency portion of the MPS powder pattern,

corresponding to the δ_{22}/δ_{33} components of the ^{195}Pt CS tensor, is abnormally broad in comparison to similar regions in the spectra of the individual reagents and MGS, increasing the associated uncertainties of CS tensor parameters, and suggesting that this region of the powder pattern may be indicative of the presence of multiple powder patterns (and multiple Pt sites). This broadening hints at additional structural information that may be contained in the powder pattern that is not resolved due to the limited resolution of the CPMG method.

^{195}Pt Hahn-echo and ^1H - ^{195}Pt CP-echo NMR experiments. In order to further investigate the δ_{22}/δ_{33} regions of the ^{195}Pt powder patterns of MPS, a series of ^{195}Pt DE Hahn-echo and ^1H - ^{195}Pt CP Hahn-echo experiments were performed. The spectra (Figure 2) were obtained with the transmitter frequency set to the approximate center of gravity of the δ_{22}/δ_{33} region, as determined from CPMG-type experiments, in order to obtain a higher-resolution pattern that may aid in resolving the discontinuities associated with multiple, overlapping powder patterns. ^{195}Pt Hahn-echo spectra of the δ_{11} regions of all compounds were also acquired in order to extract increasingly accurate ^{195}Pt CS tensor parameters (Table 1, Figure S5). Recycle delays for Hahn-echo experiments (Table S8) were experimentally optimized to ensure full recovery of equilibrium magnetization. For $\text{Pt}(\text{NH}_3)_4\text{Cl}_2 \cdot \text{H}_2\text{O}$, the Hahn-echo spectrum of the δ_{22}/δ_{33} region of the powder pattern reveals a single, sharp discontinuity, characteristic of a platinum CS tensor with $\kappa = -1$. For MGS, equivalent experiments reveal two distinct discontinuities at ca. -4725 ppm and -4770 ppm, corresponding to two separate ^{195}Pt powder patterns, which are assigned to the $[\text{Pt}(\text{NH}_3)_4]^{2+}$ and $[\text{PtCl}_4]^{2-}$ species, respectively. These assignments were made according to peak intensities: the δ_{22}/δ_{33} region with highest intensity in a DE ^{195}Pt Hahn-echo experiment arises from the $[\text{Pt}(\text{NH}_3)_4]^{2+}$ species, as it has a smaller Ω value, meaning that its powder pattern is spread over a narrower region than that of the

$[\text{PtCl}_4]^{2-}$ species. Interestingly, peak intensities obtained via ^1H - ^{195}Pt CP-echo experiments on MGS are dissimilar to those obtained via ^{195}Pt Hahn-echo experiments, the latter of which are quantitative in terms of integrated signal intensity and spin counting, provided that suitably long recycle delays are applied. Shorter ^1H - ^{195}Pt CP mixing times are more efficient for CP to the $[\text{PtCl}_4]^{2-}$ ion, while longer mixing times are more efficient for CP to the $[\text{Pt}(\text{NH}_3)_4]^{2+}$ ion; hence, integrated signal intensities are not quantitative.

In contrast to the relatively narrow δ_{22}/δ_{33} portion of the MGS powder pattern, ^1H - ^{195}Pt CP-echo experiments on MPS (Figure 2) reveal a broad region of spectral intensity punctuated by fine structure (DE experiments were unsuccessful, *vide supra*). There are two major regions of spectral intensity within the δ_{22}/δ_{33} portion of the MPS powder pattern: a higher-frequency region of generally uniform intensity which stretches from ca. -4600 to -4930 ppm, and a lower-frequency region of high signal intensity from ca. -4960 to -5150 ppm. The former region encompasses the δ_{22}/δ_{33} regions of the powder patterns of both MGS and $\text{Pt}(\text{NH}_3)_4\text{Cl}_2 \cdot \text{H}_2\text{O}$, indicating their presence as minor impurities. The latter region has shifts that do not correspond to any discontinuities from the patterns of the starting reagents or MGS. This region is also abnormally broad for a single powder pattern and appears to have subtle details which may be indicative of two distinct MPS species (i.e., two ^{195}Pt CS tensors with $\kappa \approx -1$ corresponding to $[\text{Pt}(\text{NH}_3)_4]^{2+}$ and $[\text{PtCl}_4]^{2+}$ ions). It is also important to note that none of the aforementioned spectral intensity in Figure 2 arises from any K_2PtCl_4 impurities in the MPS sample, as this would not be observed via ^1H - ^{195}Pt CP experiments.

The two-site simulation of MPS (Figure 3(a)) does not adequately account for the uniform intensity observed in the experiment from -4600 to -4930 ppm. As described above, CP experiments are clearly not quantitative, and the intensity from -4600 to -4930 ppm in the MPS spectrum is likely

due to lower concentrations of MGS and $\text{Pt}(\text{NH}_3)_4\text{Cl}_2\cdot\text{H}_2\text{O}$ impurities that are disproportionately enhanced by the CP experiment (powder XRD also indicates the presence of only trace impurities in MPS, *vide infra*). A five-site ^{195}Pt NMR simulation (Figure 3(b), Figure S6) considering various impurities in the MPS sample is able to account for most of this unassigned spectral intensity. In addition, experiments on impure MPS samples exhibit high spectral intensity in the -4600 to -4930 ppm region (Figure S7), indicating that this intensity originates from impurities and not the MPS compound itself.

^{195}Pt MAS NMR experiments. A series of DE ^{195}Pt MAS NMR experiments were performed in order to attempt to differentiate the number and nature of Pt-containing compounds within MPS via their isotropic chemical shifts. ^{195}Pt MAS NMR spectra of MGS and MPS are shown in Figure 4. Although fast spinning speeds (ca. 25 kHz) and very short 90° pulse lengths (1 μs) were employed (Table S11), the entire manifold of spinning sidebands does not appear to be uniformly excited over its entire breadth (ca. 1 MHz at 9.4 T). In addition, S/N is very low, despite the acquisition of a large number of transients. The extraction of CS tensor parameters from these spectra is very unlikely, as previously demonstrated for ^{195}Pt and ^{207}Pb CS tensor parameters extracted from very broad MAS patterns via Herzfeld Berger analysis (HBA).^{41,91} Furthermore, due to the ineffectiveness of CP at high spinning speeds, direct excitation experiments on ^{195}Pt must be applied; however, the long recycle delays and subsequent lengthy experimental times make these experiments very challenging. Despite all of this, MAS NMR experiments can be useful for identifying and refining δ_{iso} values for the individual Pt species, and potentially for the detection of multiple sites.

The ^{195}Pt MAS NMR spectrum of MGS (Figure 4(a)) reveals two distinct sets of spinning

sidebands originating from two unique Pt species. The δ_{iso} values for the $[\text{PtCl}_4]^{2-}$ and $[\text{Pt}(\text{NH}_3)_4]^{2+}$ species are unique in comparison to those of the starting reagents. We note that a calibrated recycle delay of 40 s was employed to ensure full recovery of equilibrium magnetization. The MAS spectrum of MPS (Figure 4(b)) has only one set of spinning sidebands corresponding to a single Pt species. The δ_{iso} of -2560(6) ppm is assigned to the $[\text{Pt}(\text{NH}_3)_4]^{2+}$ species based on CS tensor parameters extracted from BRAIN-CP/WCPMG experiments (vide supra). A recycle delay of 90 s was employed in a second experiment, in an attempt to observe the $[\text{PtCl}_4]^{2-}$ species, with no success (Figure 4(c)). This information, paired with the failure to obtain a proper ^{195}Pt powder pattern with direct excitation WURST-CPMG experiments, suggests that the ^{195}Pt nucleus of the $[\text{PtCl}_4]^{2-}$ species of MPS has a much longer T_1 value than that of the $[\text{PtCl}_4]^{2-}$ species of MGS. This is again consistent with the $[\text{PtCl}_4]^{2-}$ units being further away from the $[\text{Pt}(\text{NH}_3)_4]^{2+}$ units in MPS as compared to MGS, in that there is not a proximate source of mobile protons in MPS to induce faster ^{195}Pt longitudinal relaxation.

^{14}N WURST-CPMG and ^1H - ^{14}N BRAIN-CP/WCPMG experiments. Since three of the four compounds contain the $[\text{Pt}(\text{NH}_3)_4]^{2+}$ ion, ^{14}N SSNMR experiments were performed in an attempt to elicit additional structural information. ^{14}N is a quadrupolar nucleus with a spin of 1, and is usually associated with SSNMR spectra that are dominated by the first-order quadrupolar interaction (FOQI).^{92,93} In comparison to the FOQI, the effects of nitrogen CSA on ^{14}N SSNMR spectra are minimal, and no nitrogen CS tensor parameters or δ_{iso} values could be determined for these systems. However, since the powder patterns are Pake doublets with mirror symmetry, the complete ^{14}N NMR spectra were generated by “reflecting” the low-frequency (right) portion of the powder pattern about $\delta = 0$ ppm (see Experimental section).⁵⁸

The ^{14}N SSNMR spectra are shown in Figure 5, and the corresponding EFG tensor parameters are summarized in Table 2. Initially, ^{14}N direct-excitation WURST-CPMG experiments were performed (Figure 5, left), but unfavourably long $T_1(^{14}\text{N})$ values resulted in long experimental times (Table S5). The lengthy experimental times also limited the resolution with which the spectra could be acquired; as a result, the accuracy of the quadrupolar parameters extracted from these spectra is questionable. ^1H - ^{14}N BRAIN-CP/WCPMG experiments were subsequently used to acquire spectra (Figure 5, right), yielding substantial increases in both S/N and spectral resolution and concomitant decreases in experimental times (Table S7) due to the relatively short $T_1(^1\text{H})$ values. All spectra are approximately between 1500 and 1700 kHz wide at 9.4 T and exhibit well-defined features, correlating to relatively axially symmetric ^{14}N EFG tensors with η_Q values ranging from 0.02 to 0.15 and C_Q values between 1.00 and 1.20 MHz.

The most striking difference between the WURST-CPMG and BRAIN-CP/WCPMG spectra are the apparent number of powder patterns arising from the $\text{Pt}(\text{NH}_3)_4\text{Cl}_2 \cdot \text{H}_2\text{O}$ and MGS samples. WURST-CPMG experiments seem to indicate only one powder pattern for each of these compounds, while BRAIN-CP/WCPMG experiments indicate that there are two distinct powder patterns for each. Both types of experiments indicate that the MPS sample gives rise to a single powder pattern. The origin of the discrepancy in observed powder patterns for $\text{Pt}(\text{NH}_3)_4\text{Cl}_2 \cdot \text{H}_2\text{O}$ and MGS in these experiments lies in the differences in T_1 relaxation times between the two ^{14}N environments. Since only one powder pattern is observed in direct-excitation WURST-CPMG experiments, the other unobserved powder pattern must be associated with a ^{14}N environment with a much longer T_1 value. When ^1H - ^{14}N BRAIN-CP/WCPMG experiments are employed, both powder patterns are observed, owing to the reliance of these experiments on the uniformly short $T_1(^1\text{H})$ values rather than the

disparate $T_1(^{14}\text{N})$ values.

Both the ^{14}N WURST-CPMG and the ^1H - ^{14}N BRAIN-CP/WCPMG pulse sequences produce spectra that exhibit a characteristic “dip” in the center of the ^{14}N powder patterns (i.e., a lack of experimental spectral intensity in comparison to the simulated idealized powder pattern). This dip is particularly pronounced in spectra produced from ^1H - ^{14}N BRAIN-CP/WCPMG experiments, and the origins of such a dip may be related to a population transfer mechanism we have described previously.⁹⁴ We stress that it is not crucial to obtain the spectral intensity in the center of these symmetrical powder patterns, since the ^{14}N quadrupolar parameters depend only upon the positions of the three diagnostic features (horn, shoulder, and foot), which are undistorted, well-resolved, and separated from the center of these powder patterns by a relatively large gap in frequency.

The ^{14}N powder patterns of $\text{Pt}(\text{NH}_3)_4\text{Cl}_2\cdot\text{H}_2\text{O}$ and MGS correspond to two unique, but similar, EFG tensors. As noted elsewhere, ^{14}N EFG tensors are sensitive to inter- and intra-molecular hydrogen bonding interactions involving nitrogen-bound protons,^{92,95-97} and subtle differences in the strength of these interactions leads to differences in ^{14}N EFG tensor parameters. In similar square planar Pt(II) systems containing amine groups, the EFG tensor is generally axially symmetric (i.e., $\eta_Q \approx 0$) and its principal component with the largest absolute magnitude, V_{33} , is oriented on or near the threefold axis of rotational symmetry (C_3 axis) coincident with the Pt-N bond, while V_{22} and V_{11} are perpendicular to this axis.⁴¹ The C_3 rotational symmetry may be disrupted by hydrogen bonding involving amine protons, which results in a loss of axial symmetry of the EFG tensor and corresponding non-zero η_Q values.⁹⁵

In the case of $\text{Pt}(\text{NH}_3)_4\text{Cl}_2\cdot\text{H}_2\text{O}$, our ab initio geometry-optimized structure (more reliable than the crystal structure, vide supra) predicts that two crystallographically unique ^{14}N sites, N1 and

N2, are present due to a very subtle deviation from a D_{4h} square planar geometry about Pt. The deviation from square planar symmetry is slight, with $\angle N1-Pt-N2 = 88.95^\circ$, $\angle N2-Pt-N1 = 91.05^\circ$, torsion angle $\angle N1-Pt-N2-N1 \approx 1^\circ$, and difference of 0.002 Å in Pt-N1 and Pt-N2 bond length. Such differences, however, give rise to distinct N-H...Cl distances for each nitrogen site (Table S13, Figure S10). With regard to N1, the relatively shorter N1-H...Cl distances lead to hydrogen bonding which disrupts the C_3 rotational symmetry about the Pt-N1 bond, resulting in a ^{14}N EFG tensor of lower axial symmetry (higher η_Q of 0.15) compared to the tensor associated with the N2 crystallographic site (lower η_Q of 0.02).

The reported MGS crystal structure indicates one unique ^{14}N site,²⁷ however, it is very likely that small deviations from ideal D_{4h} square planar symmetry are present, as in $Pt(NH_3)_4Cl_2 \cdot H_2O$. The ^{14}N BRAIN-CP/WCPMG spectrum of MGS indicates the presence of two similar ^{14}N EFG tensors, differentiated via local N-H...Cl hydrogen-bonding (η_Q values of 0.12 and 0.005). The distinction between crystallographic nitrogen sites in MGS, as represented by the ^{14}N EFG tensors, is less pronounced than in the $Pt(NH_3)_4Cl_2 \cdot H_2O$ system, possibly owing to the nature of Cl atoms in these systems (i.e., Cl is covalently bound to Pt in MGS but is a counter-ion in $Pt(NH_3)_4Cl_2 \cdot H_2O$, which may result in distinct hydrogen bonds in the latter).

The ^{14}N SSNMR spectrum of MPS displays a single powder pattern, from which values of C_Q of 1.00 MHz and η_Q of 0.07 are determined. The ^{14}N EFG tensor parameters of the ^{14}N sites in MPS are similar to the compounds discussed previously, and indicate that the $[Pt(NH_3)_4]^{2+}$ ion is intact within MPS. The absence of a distinct second ^{14}N powder pattern provides clear evidence that the structure of MPS is quite different from that of $Pt(NH_3)_4Cl_2 \cdot H_2O$ and MGS, and that any deviations from D_{4h} symmetry in the $[Pt(NH_3)_4]^{2+}$ species within MPS must be extremely small. The

MPS ^{14}N EFG tensor displays a non-zero η_Q value that, when compared to MGS and $\text{Pt}(\text{NH}_3)_4\text{Cl}_2\cdot\text{H}_2\text{O}$ ^{14}N EFG tensors, suggests that amine groups in MPS may be involved in hydrogen bonding with nearby Cl atoms (as in the case of the site N2 nitrogens in $\text{Pt}(\text{NH}_3)_4\text{Cl}_2\cdot\text{H}_2\text{O}$). Perhaps most importantly, both the ^{14}N and ^{195}Pt NMR data suggest that the long range structure of MPS may be very different from those of MGS and the starting reagents, and that there may be very different unit cell parameters and space group symmetry.

^{35}Cl WURST-CPMG experiments. In order to verify the presence of $[\text{PtCl}_4]^{2-}$ units within MPS and investigate their local environments, ^{35}Cl SSNMR experiments were performed on all of the Pt complexes. There are two NMR active chlorine isotopes, ^{35}Cl and ^{37}Cl , which both have nuclear spins of $I = 3/2$, moderately sized nuclear quadrupole moments, and relatively low gyromagnetic ratios (they are classified as low- γ nuclides). The former is generally preferred for SSNMR studies, due to its higher natural abundance. ^{35}Cl SSNMR powder patterns are typically dominated by the second-order quadrupolar interaction (SOQI), whose nature depends solely on the electric field gradients (EFG) about the ^{35}Cl nucleus; however, for narrower patterns arising from smaller C_Q values, the effects of chlorine chemical shift anisotropy (CSA) can often be observed. The breadth of the central transition (CT) of the ^{35}Cl SSNMR pattern scales inversely with magnetic field; hence, it is advantageous to utilize a field of 21.1 T for all ^{35}Cl NMR experiments. The majority of reports on ^{35}Cl SSNMR have dealt with ionic chlorine species with relatively narrow patterns and correspondingly small nuclear quadrupolar coupling constants, C_Q .⁹⁸⁻¹⁰³ Recently, ^{35}Cl UW NMR experiments have been applied to study chlorine atoms in terminal and bridging bonding environments in transition metal complexes, as well as in terminal carbon-chlorine bonds in organic molecules, where powder patterns can be over several MHz in breadth.^{41,104-109}

The ^{35}Cl SSNMR spectra for all compounds are shown in Figure 6 and the corresponding EFG tensor parameters are presented in Table 3. The ^{35}Cl NMR powder pattern for $\text{Pt}(\text{NH}_3)_4\text{Cl}_2\cdot\text{H}_2\text{O}$ (Figure 6(b)) is very narrow in comparison to those of all the other systems and arises from a single unique site. The Cl^- ions in $\text{Pt}(\text{NH}_3)_4\text{Cl}_2\cdot\text{H}_2\text{O}$ are not involved in any covalent bonds; hence, ^{35}Cl nuclei in such environments experience small EFGs, and correspondingly, have small C_Q values. The remainder of the systems have very broad patterns and large values of C_Q , since the Cl atoms therein are involved in covalent bonds. Since the magnitude of the quadrupolar interactions in these systems is very large in comparison to the spans of the chemical shift (CS) tensors, it is impossible to extract any ^{35}Cl CS tensor information except for very rough estimates of δ_{iso} , even when utilizing a traditional Hahn-echo experiment.

The ^{35}Cl SSNMR spectra of K_2PtCl_4 and MGS yield EFG tensor parameters that are identical within experimental uncertainty, indicating that their respective $[\text{PtCl}_4]^{2-}$ units reside in similar environments (i.e., distinct Pt-Pt metallophilic interactions do not drastically alter the electronic structure of the Pt-Cl bonds). In agreement with their reported crystal structures, the $[\text{PtCl}_4]^{2-}$ units within K_2PtCl_4 and MGS each give rise to a single ^{35}Cl powder pattern.

The ^{35}Cl powder pattern of MPS has two unique powder patterns (1:1 integrated intensity ratio), both with EFG tensors similar to those of K_2PtCl_4 and MGS. The sharp resonance at ca. 100 ppm is attributed to a small amount of $\text{Pt}(\text{NH}_3)_4\text{Cl}_2\cdot\text{H}_2\text{O}$ reagent. The spectral features in this spectrum are not as sharp as in those of MGS and K_2PtCl_4 . This may indicate a slightly lower degree of crystallinity within the MPS sample or minor contamination from the MGS co-product and K_2PtCl_4 reagent (as suggested by ^{195}Pt SSNMR spectra); however, these impurities are not evident in the ^{35}Cl SSNMR spectrum of MPS. As an illustration of the sensitivity of ^{35}Cl SSNMR to

impurities in the MPS system, the ^{35}Cl SSNMR spectrum of an impure sample yields one narrow and three broad powder patterns, readily indicating the presence of MGS, K_2PtCl_4 , and $\text{Pt}(\text{NH}_3)_4\text{Cl}_2\cdot\text{H}_2\text{O}$ impurities (Figure S11).

The columnar structures of K_2PtCl_4 and MGS give rise to a single ^{35}Cl SSNMR powder pattern, indicative of a sole ^{35}Cl crystallographic site, while spectra of MPS indicate two ^{35}Cl sites. The existence of two unique yet similar chlorine sites in MPS may be due to a subtle shift away from idealized symmetry about the $[\text{PtCl}_4]^{2-}$ square planar center, or some other structural difference. This data, along with ^{195}Pt and ^{14}N results, further suggests a structure that is distinct from the common columnar or stacked square-planar Pt motif.

Powder X-ray diffraction experiments and refinement of MPS data. To further investigate the unique MPS structure suggested by SSNMR, pXRD patterns were acquired for all compounds (Figure 7). Powder XRD experiments were completed at Beamline X7B of Brookhaven National Laboratory. The sharp peaks in each diffraction pattern are consistent with highly crystalline samples, although the slightly broader peaks in the pattern of MPS infer a lower degree of crystallinity, consistent with NMR observations. The powder patterns obtained for K_2PtCl_4 , $\text{Pt}(\text{NH}_3)_4\text{Cl}_2\cdot\text{H}_2\text{O}$, and MGS agree well with calculated powder patterns based on reported crystal structures (Figure S12). The powder diffraction patterns for the MPS samples clearly indicate that MPS is the major product of our synthesis, with minor peaks (i.e., $2\theta \approx 3^\circ$) corresponding to MGS and small amounts of the starting reagents. Two separate batches of MPS were analyzed; both NMR spectra and pXRD patterns indicate that MGS and reagents are limited to minor impurities in both cases, demonstrating the reproducibility of our synthesis.

Rietveld refinements and Le Bail fittings were attempted on the MPS X-ray diffraction data.

The relatively low crystallinity of the MPS samples and presence of multiple trace impurities results in reduced resolution of the high-angle diffraction peaks; hence, a full set of crystal structure parameters could not be determined. However, since Pt is associated with > 90% of electron density within MPS, a reasonable fit of experimental diffraction data was obtained by only accounting for Pt atomic positions (Figure 8). Fortunately, some of the crucial details of the MPS crystal structure can be reported from this refinement (Table 4). Notably, MPS crystallizes in a body-centered tetrahedral crystal structure (space group $I4$), with $a = b = 5.576 \text{ \AA}$ and $c = 8.174 \text{ \AA}$. The electron density map obtained from the refinement of the pXRD data indicates that the structure of MPS is very different from those of all of the other species discussed herein (Figure 9). The square planar units are no longer arranged in linear columns with short Pt-Pt distances. The intermolecular Pt-Pt columnar stacking distance obtained from the refinement is 8.174 \AA , consistent with the prediction of a distance $> 5 \text{ \AA}$,²⁷ and far longer than the MGS Pt-Pt distance of 3.25 \AA . Most importantly, the closest Pt-Pt distance of 5.576 \AA in the MPS crystal structure lies between adjacent parallel square planar units along the a and b axes, a structural arrangement that clearly prohibits any Pt-Pt orbital overlap or metallophilic interactions.

Analysis of the MPS electron density map indicates that Pt atoms are square planar coordinated to four ligands, and although most of their electron density could be localized, their identities and exact locations could not be accurately determined. Attempts to incorporate Cl or N positions resulted in no appreciable increase in fit accuracy (Figure S13). Undoubtedly, the intrinsically poor crystallinity of MPS and the presence of trace impurities prevent identification of the electron density source from pXRD methods alone. X-ray absorption fine structure experiments were employed to investigate the identity and coordination of Pt ligands in MPS.

X-ray absorption fine structure experiments. The reader is directed to the Supporting Information, Appendix A, for detailed data and accompanying figures regarding XANES and EXAFS experiments; herein only key findings are briefly discussed. XANES spectra of the Pt complexes have the same position for the absorption edge, which indicates that the Pt atoms in both MPS and MGS are of the same oxidation state as $\text{Pt}(\text{NH}_3)_4\text{Cl}_2 \cdot \text{H}_2\text{O}$, which was used as a reference. The EXAFS analysis provides information regarding the local environment of Pt in MPS, with specific focus on ligand coordination to Pt. The fitting results of the Pt L_{III} edge confirm the presence of Pt-N and Pt-Cl bonds in MPS and indicate bond lengths of 2.032(0.013) and 2.300(0.007) Å, respectively; these bond lengths are similar to the 2.036(0.020) and 2.310(0.010) Å obtained from a sample of MGS.

Proposed structural model of MPS. ^{195}Pt , ^{35}Cl , and ^{14}N SSNMR data can be used in conjunction with pXRD and EXAFS results in order to formulate a clear structural model of MPS (Figure 10). X-ray diffraction experiments provide the location of the Pt atoms within the MPS unit cell as well as crucial unit cell parameters, and ^{195}Pt , ^{14}N , and ^{35}Cl SSNMR spectra indicate that the Pt atoms are in square planar $[\text{Pt}(\text{NH}_3)_4]^{2+}$ and $[\text{PtCl}_4]^{2-}$ units. Within MPS, the Pt units stacked in a columnar fashion along the crystallographic c axis are composed of a sole Pt species with interlayer Pt-Pt distances of 8.174 Å, rather than the alternating $[\text{Pt}(\text{NH}_3)_4]^{2+}$ and $[\text{PtCl}_4]^{2-}$ units separated by 3.25 Å observed in MGS. The long Pt-Pt distance, in conjunction with ^{195}Pt SSNMR experiments, indicate that there are no Pt-Pt contacts present within MPS. The presence of a sole ^{14}N SSNMR powder pattern indicates that the $[\text{Pt}(\text{NH}_3)_4]^{2+}$ units within MPS assume nearly ideal D_{4h} square planar symmetry. Likewise, the two similar powder patterns observed via ^{35}Cl SSNMR of MPS hint that the $[\text{PtCl}_4]^{2-}$ units exhibit a subtle deviation from square planar geometry. EXAFS data indicate

that Pt-N and Pt-Cl bond distances within MPS are similar to those of MGS. With a structural determination of MPS complete, computations on a selection of platinum compounds should be able to provide insight into the experimental ^{195}Pt CS tensor parameters.

First principles calculations. In this section, DFT calculations of platinum nuclear magnetic shielding (MS) tensors are presented for several model cluster compounds for $\text{Pt}(\text{NH}_3)_4\text{Cl}_2\cdot\text{H}_2\text{O}$, K_2PtCl_4 and MGS. As discussed in the experimental section, calculations on MPS are excluded from the current work, due to difficulties in obtaining a model cluster compound that yielded a satisfactorily converged ground state. Model clusters (Figure 11) were initially constructed from atomic coordinates based on known crystal structures; geometry optimizations of the atomic positions were performed with periodic boundary conditions, as described in the experimental section.

The platinum isotropic nuclear shielding constants, σ_{iso} , calculated with scalar (SC) and spin-orbit (SO) ZORA methods are collected in Table 5. The relative CS and MS values are given in Table 6. Examination of the differences in δ_{iso} and σ_{iso} among the various species in Table 6 reveal that the SO calculations provide slightly better quantitative agreement with experiment. This is especially clear in comparing the data for the two possible structural models for K_2PtCl_4 : both have the $[\text{K}_8(\text{PtCl}_4)_3]^{2+}$ cluster, but feature slightly different Pt-Cl bond lengths (model **B**: 2.337 Å (geometry optimized value), model **B'**: 2.309 Å (crystal structure)).⁷⁷ In particular, the **B'** model yields differences in σ_{iso} that are closer to the experimental δ_{iso} differences. The variation in σ_{iso} resulting from the small changes in Pt-Cl bond lengths is unsurprising, as this has been previously observed in similar calculations on Pt model compounds.^{67,69}

The platinum MS tensor components for the cluster models are given in Table 7.

Comparison of the spans of the CS and MS tensors also shows good quantitative agreement; interestingly, the results for the **B** cluster are superior to those of **B'** in this case. The skews of each tensor are all near or equal to -1.0 (i.e., σ_{11} is distinct and $\sigma_{22} \approx \sigma_{33}$), in good agreement with experimental data. Polar plots of the anisotropic MS tensors for K_2PtCl_4 and the PtCl_4^{2-} unit of MGS (Figure 12) feature blue and orange regions indicating directions of positive and negative magnetic shielding, respectively. The surfaces show the magnetic shielding response magnitude as a function of the magnetic field direction and indicate the magnitude, sign, and orientation of the tensor principal components:^{110,111} hence, σ_{11} is oriented perpendicular to the square plane, and σ_{22} and σ_{33} are contained within the square plane, consistent with our arguments based on the experimental CS tensors and local symmetry of each Pt site. The MS tensors in the $\text{Pt}(\text{NH}_3)_4^{2+}$ units are similarly oriented (Figure S14). Perhaps most importantly, it is the σ_{11}/δ_{11} parameters that show the strongest differences with structural variation. Notably, decreases in Pt-Pt distances in the “columnar” complexes (i.e., the starting reagents and MGS) correspond to decreased (more negative) shielding along the direction of σ_{11}/δ_{11} (i.e., the direction of the Pt-Pt interactions).

It is of great importance to understand the relationships between differences in electronic structure and the platinum MS parameters. The results of a localized molecular orbital (LMO) analysis of platinum magnetic shielding are presented in Tables 8 and S15-17. There are three main classes of LMOs under consideration: Pt non-bonding *5d* orbitals (referred to in Table 8 as “lone pairs” (LPs)), Pt-ligand bonds and Pt core orbitals. It has previously been shown that it is the *5d* orbitals that cause the largest variations in MS in Pt(II) versus Pt(IV) complexes.⁶⁸ They may also outweigh the latter two classes of LMOs in determining the trends in MS among Pt systems of a given oxidation state. This is precisely the case for our samples. The analysis shows that the

contributions to platinum MS from other distant Pt atoms and the counterions (where applicable) are minimal.

The first four rows of Table 8 list the sum totals of contributions to σ_{iso} from LMOs centered on the central Pt units of the clusters considered (Figure 11), unoccupied LMOs, and orbitals localized on the counterions and remaining Pt units, respectively. The two columns furthest to the right show the differences in MS between the $\text{Pt}(\text{NH}_3)_4^{2+}$ and PtCl_4^{2-} units in MGS and the starting reagents, respectively. It is clear that the contributions from Pt-centered LMOs dominate; these are broken down and listed in the second portion of the table (rows 5-11) in terms of Pt core MOs, Pt-ligand bonding, ligand-centered, and non-bonding $5d$ Pt orbitals (LPs).

The d_{xy} , d_{xz} and d_{yz} orbitals account for the largest contributions to deshielding of the Pt nuclei in the $\text{Pt}(\text{NH}_3)_4^{2+}$ and PtCl_4^{2-} species of the starting reagents and even more so for MGS. The d_{z^2} orbital is responsible for large shielding contributions for both species in MGS, and relatively minor shielding contributions for the starting reagents. The overall result is a larger net deshielding of the ^{195}Pt nuclei in both the $\text{Pt}(\text{NH}_3)_4^{2+}$ and PtCl_4^{2-} moieties in MGS with respect to the starting reagents.

In previous work, Autschbach and Zheng have shown that large differences in the Pt shielding between square-planar Pt(II) and octahedral Pt(IV) complexes can be traced back to the paramagnetic current density induced by the external field in the Pt $5d$ shell, which causes Pt deshielding of thousands of ppm in magnitude.⁶⁸ We adopt an “orbital rotation model” for d orbitals for the following discussion.^{68,112} The major MS contribution of the d_{xy} orbital (assumed to be in-plane in this case) in comparison to all of the other orbitals can be understood by considering the effects of a “rotation” caused by the perturbation by an external magnetic field along the z -direction (for diagrams of the canonical $5d$ Pt orbitals, see Figure S15). In particular, a rotated d_{xy} orbital

overlaps with unoccupied equatorial (in-plane) σ^* orbitals (anti-bonding, Pt-ligand LMOs), producing the only very large deshielding contribution along the z -direction (also the direction of σ_{11}/δ_{11} , Table S16). The d_{xz} and d_{yz} orbitals are rotated in a similar manner by magnetic fields along the y - and x -directions of the molecular frame, respectively; however, only two of the lobes of in each case align with equatorial σ^* orbitals, while the other two lobes do not (N.B., the other magnetic field components result in rotated orbitals of π and δ symmetry with respect to the ligand; contributions to the MS from mixings involving such orbitals are small in σ -bonded Pt complexes). Individually, the contributions to deshielding of the d_{xz} and d_{yz} orbitals are less than half that of the d_{xy} orbital, and are directed within the square plane (Table S17). Interestingly, these deshielding contributions are partially “counteracted” by shielding contributions involving rotation of the d_{z^2} orbital by the same magnetic fields (Tables S16-S17).

The in-plane (σ_{22} , σ_{33}) as well as the out-of-plane (σ_{11}) MS tensor components are more negative in MGS (more deshielded) than in the starting reagents. This applies to both the PtCl_4^{2-} and the $\text{Pt}(\text{NH}_3)_4^{2+}$ moieties in MGS. Individually, the σ_{11} tensor components are most strongly altered in MGS compared to the starting reagents. Tables S16 and S17 show that the more negative σ_{11} and the more negative σ_{22} , σ_{33} all contribute negative several hundred ppm to the more deshielded *isotropic* MS. The LMO analysis shows that the increased deshielding in MGS does not result from major contributions from anything other than the Pt $5d$ orbitals via the magnetic field-induced mixing discussed above. The mechanism appears to be rather general; both Pt centers in MGS are more deshielded, and the effect shows up in all of the principal components of the MS tensor. The question is: what is different between the starting reagents and MGS?

The case is best illustrated by considering an isolated 4-coordinate square planar PtX_4 system,

with X being a σ -donating ligand such as a halide or an amine. As previously shown in the literature, a corresponding six-coordinate complex PtX_6 has a much more strongly deshielded Pt center because of additional low-energy unoccupied σ^* orbitals in the direction of σ_{11} . The orbital rotation model explains why the in-plane (σ_{22} , σ_{33}) MS tensor components are more negative: the magnetic field-rotated d_{xz} and d_{yz} orbitals can overlap with the new σ^* orbitals, causing a deshielding induced paramagnetic current density at the Pt center. For a qualitative illustration, see Figure 13, where we can see the potential influence of orbital interactions between different Pt centers in MGS. There are two major differences when comparing a Pt center in MGS versus PtX_6 : (i) The orbital interactions are evidently much weaker in MGS, and (ii) linear combinations of low-energy Pt-Y σ^* orbitals in a neighboring PtY_4 unit give low-energy orbitals of σ^* , π^* , and δ^* symmetry when classified with respect to the Pt-Pt axis. As a consequence, in-plane and out-of-plane $5d$ orbitals contribute to the deshielding of the Pt center in MGS relative to the starting reagents, affecting all MS tensor components. Moreover, this model explains the sizable deshielding contributions of the Pt $5d_{z^2}$ orbitals in the σ_{22} , σ_{33} tensor components found in the LMO analysis: as Figure S15 clearly shows, the rotated orbital requires interactions of π symmetry in the σ_{11} direction to create effective paramagnetic shielding tensor contributions.

The distance to the neighboring Pt centers has a crucial influence on the platinum MS tensor. MGS, with its comparatively shorter Pt-Pt contacts, affords the orbital interactions described above that result in net deshielding along the direction of σ_{11} . Keeping in mind that at larger distances orbital interactions decrease exponentially, the Pt-Pt distances in the starting materials are too large to give significant orbital interactions in the σ_{11} direction. In MPS, the distances between Pt centers are even larger, hence its MS parameters are similar to those of the starting reagents.

Conclusions

Multinuclear SSNMR has been used in conjunction with complementary pXRD and XANES/EXAFS experiments to investigate the structure of Magnus' green and pink salts, $[(\text{Pt}(\text{NH}_3)_4][\text{PtCl}_4]$, as well as their precursors, $\text{Pt}(\text{NH}_3)_4\text{Cl}_2 \cdot \text{H}_2\text{O}$ and K_2PtCl_4 . In order to produce MPS with only a minimum of MGS co-product, a new synthetic procedure employing acetone and water was implemented. All methods of characterization, including SSNMR and pXRD, indicate our product is composed largely of the pink salt with small amounts of impurities in the form of the green salt and starting reagents. ^{195}Pt static WURST-CPMG, BRAIN-CP/WCPMG, Hahn-echo, and MAS SSNMR experiments show that the ^{195}Pt CS tensor is sensitive to the presence of Pt-Pt metallophilic interactions in these systems, and that MPS does not feature such interactions. ^{14}N and ^{35}Cl WURST-CPMG SSNMR experiments illustrate the sensitivity of EFG tensor parameters to small deviations from ideal D_{4h} square planar symmetry in the $\text{Pt}(\text{NH}_3)_4\text{Cl}_2$ and K_2PtCl_4 compounds, and such experiments also confirm that Magnus' pink salt is composed of square planar $[\text{Pt}(\text{NH}_3)_4]^{2+}$ and approximately square planar $[\text{PtCl}_4]^{2-}$ units. A Rietveld refinement of MPS diffraction data resulted in elucidation of several important crystal structure parameters, including the space group, the unit cell parameters, and the atomic positions of Pt. EXAFS experiments indicate that the Pt-N and Pt-Cl bond lengths within MPS are similar to those of MGS. The crystal structure of MPS features a non-columnar arrangement of square planar Pt units; this motif is unique from that of MGS and the reagents, and precludes any possibility of metallophilic Pt-Pt interactions within MPS. First-principles calculations were performed in order to correlate NMR parameters and molecular structure, and confirm that differences in out-of-plane nuclear magnetic shielding give rise to the unique MGS ^{195}Pt SSNMR spectra. The unique structure of MPS, with its absence of Pt-Pt

metallophilic interactions, has CS tensors that are similar to starting reagents, consistent with these theoretical models of MS tensor contributions. With conclusive evidence that the ^{195}Pt CS tensor is sensitive to Pt-Pt interactions, we plan to employ this combination of ultra-wideline SSNMR along with pXRD techniques to extend our study across a variety of Pt-based systems with Pt-Pt contacts.

Acknowledgements

B EGL thanks the Ontario Ministry of Training, Colleges, and Universities for a Queen Elizabeth II Ontario Graduate Scholarship in Science and Technology (QEII-GSST). RWS thanks the Natural Sciences and Engineering Research Council (NSERC, Canada), the Canadian Foundation for Innovation, the Ontario Innovation Trust and the University of Windsor for support. RWS also thanks the Ontario Ministry of Research and Innovation for an Early Researcher Award, and acknowledges the Centre for Catalysis and Materials Research (CCMR) at the University of Windsor for additional funding. Dr. Kris J. Harris and Mr. Stanislav Veinberg are acknowledged for their assistance with BRAIN-CP/WCPMG experiments. Prof. Walter Caseri (Swiss Federal Institute of Technology Zurich) is thanked for very helpful comments regarding the synthesis of MPS.

Access to the 900 MHz NMR spectrometer was provided by the National Ultrahigh-Field NMR Facility for Solids (Ottawa, Canada), a national research facility funded by the Canada Foundation for Innovation, the Ontario Innovation Trust, Recherche Québec, the National Research Council Canada, and Bruker BioSpin and managed by the University of Ottawa (www.nmr900.ca). The Natural Sciences and Engineering Research Council of Canada (NSERC) is acknowledged for a Major Resources Support grant. We are grateful to Dr. Victor Terskikh and Dr. Eric Ye for experiments run at the National Ultrahigh-field NMR Facility.

The National Synchrotron Light Source is funded by the U.S. Department of Energy, Office of Science, Office of Basic Energy Sciences, under Contract DE-AC02-98CH10886.

This work has been supported by grant CHE 0952253 from the National Science Foundation. MS is grateful for financial support from the Ministry of Science and Higher Education in Poland (“Mobility Plus” program) and from the Foundation for Polish Science (“START” scholarship). The

authors would like to acknowledge the Center for Computational Research (CCR) at the University at Buffalo for providing computational resources. MS thanks Dr. James Hooper for some technical advice.

Supporting Information. Detailed EXAFS and XANES analysis, tabulated results of FT-IR, elemental analysis, and ^1H MAS SSNMR experiments, additional SSNMR spectra, complete SSNMR experimental parameters, pXRD refinement parameters for MGS, illustrations of calculated Pt magnetic shielding in $\text{Pt}(\text{NH}_3)_4\text{Cl}_2 \cdot \text{H}_2\text{O}$ and MGS, detailed Pt LMO and NLMO contributions to Pt magnetic shielding. This material is available free of charge via the Internet at <http://pubs.acs.org>.

Table 1. Platinum chemical shift tensor parameters determined from ^{195}Pt static and MAS NMR experiments.^a

Compound	Method ^b	δ_{11} (ppm)	δ_{22} (ppm)	δ_{33} (ppm)	δ_{iso} (ppm) ^c	Ω (ppm) ^d	κ ^e
$\text{K}_2\text{PtCl}_4$⁵⁰							
	W	5385(90)	-4879(77)	-5035(77)	-1510(60)	10420(100)	-0.97(1)
$\text{Pt}(\text{NH}_3)_4\text{Cl}_2 \cdot \text{H}_2\text{O}$							
	E	2254(39)	-4928(29)	-4946(27)	-2540(20)	7200(50)	-0.995(5)
	CE	2254(39)	-4928(29)	-4946(27)	-2540(20)	7200(50)	-0.995(5)
	W	2245(90)	-4860(72)	-5005(70)	-2540(60)	7250(100)	-0.96(1)
	M	2160(550)	-4840(628)	-4840(374)	-2507(10)	7000(700)	-0.99(1)
Green Salt $[\text{PtCl}_4]^{2-}$							
	E	6630(25)	-4770(40)	-4770(40)	-970(15)	11400(30)	-1.00(1)
	W	6563(90)	-4737(102)	-4737(102)	-970(60)	11300(100)	-1.00(2)
	BC	6563(52)	-4737(57)	-4737(57)	-970(40)	11300(50)	-1.00(1)
	M	-	-	-	-970(6)	-	-
Green Salt $[\text{Pt}(\text{NH}_3)_4]^{2+}$							
	E	2835(22)	-4725(27)	-4725(27)	-2205(10)	7560 (30)	-1.00(1)
	W	2795(90)	-4705(85)	-4705(85)	-2205(60)	7500(100)	-1.00(2)
	BC	2828(52)	-4722(50)	-4722(50)	-2205(40)	7550(50)	-1.00(1)
	M	-	-	-	-2208(6)	-	-
Pink Salt $[\text{PtCl}_4]^{2-}$							
	CE	5530(48)	-5045(49)	-5045(39)	-1520(30)	10575(50)	-1.00(1)
	BC	5473(91)	-4975(77)	-5028(71)	-1510(60)	10500(100)	-0.99(1)
Pink Salt $[\text{Pt}(\text{NH}_3)_4]^{2+}$							
	CE	2367(29)	5014(26)	-5033(23)	-2560(20)	7400(30)	-0.995(5)
	BC	2373(84)	-5027(65)	-5027(61)	-2560(50)	7400(100)	-1.00(1)
	M	-	-	-	-2560(6)	-	-

^a The uncertainties in δ_{iso} , Ω , and κ were measured from experimental spectra and corresponding simulations. The uncertainties in individual CS tensor components (δ_{11} , δ_{22} , δ_{33}) were mathematically propagated from the formulae used to calculate δ_{iso} , Ω , and κ . ^b E = Hahn echo experiment, W = WURST-CPMG experiment, M = MAS experiment, CE = ^1H - ^{195}Pt cross-polarized Hahn echo experiment, BC = ^1H - ^{195}Pt BRAIN-CP/WCPMG experiment. ^c Isotropic chemical shift: $\delta_{\text{iso}} = (\delta_{11} + \delta_{22} + \delta_{33})/3$.

^d Span: $\Omega = \delta_{11} - \delta_{33}$. ^e Skew: $\kappa = 3(\delta_{22} - \delta_{\text{iso}})/\Omega$.

Table 2. Experimental ^{14}N EFG tensor parameters.

Compound	Method ^a	Site (% Intensity) ^b	$ C_Q $ (MHz) ^c	η_Q ^d
$\text{Pt}(\text{NH}_3)_4\text{Cl}_2 \cdot \text{H}_2\text{O}$	W		1.04(5)	0.15(5)
	BC	N1 (33)	1.19(2)	0.02(2)
	BC	N2 (100)	1.03(2)	0.15(2)
Magnus' Green Salt	W		1.14(6)	0.04(6)
	BC	N1 (25)	1.14(2)	0.005(5)
	BC	N2 (100)	1.11(2)	0.12(2)
Magnus' Pink Salt	W		1.06(6)	0.11(6)
	BC		1.00(2)	0.07(2)

^a W = WURST-CPMG experiment, BC = ^1H - ^{14}N BRAIN-CP/WCPMG experiment. ^b ^{14}N powder patterns obtained using BRAIN-CP/WCPMG require simulation using different relative intensities due to differences in ^1H - ^{14}N cross-polarization efficiency between the two unique nitrogen environments.

^c Quadrupolar coupling constant: $C_Q = eQV_{33}/h$, where the principal components of the EFG tensor are defined as $|V_{33}| \geq |V_{22}| \geq |V_{11}|$. Only the absolute values of C_Q can be obtained from the NMR powder patterns, not their signs. ^d Asymmetry parameter: $\eta_Q = (V_{11} - V_{22})/V_{33}$.

Table 3. Experimental ^{35}Cl NMR parameters.^a

Compound	Site	$ C_Q $ (MHz) ^{b, c}	η_Q ^d	δ_{iso} (ppm)
K_2PtCl_4		35.7(2)	0.09(1)	-125(75)
$\text{Pt}(\text{NH}_3)_4\text{Cl}_2 \cdot \text{H}_2\text{O}$		1.85(5)	0.30(5)	100(5)
Magnus' Green Salt		35.6(2)	0.095(10)	-125(75)
Magnus' Pink Salt	1	33.8(2)	0.11(1)	0(75)
	2	35.1(1)	0.10(1)	0(75)

^a All ^{35}Cl NMR experiments were conducted at a magnetic field strength of 21.1 T. $\text{Pt}(\text{NH}_3)_4\text{Cl}_2$ was acquired using a Hahn-echo pulse sequence, all other spectra were acquired using the WURST-CPMG pulse sequence. ^b These ^{35}Cl spectra are dominated by the second-order quadrupolar interaction, making quantification of the relatively smaller contributions from the chlorine CSA impossible in all cases. ^{c, d} See definitions given in footnotes *c* and *d* in Table 2.

Table 4. Powder X-ray diffraction refinement parameters of Magnus' Pink Salt crystal structure.

Atomic Position Parameters - Pt ^a	
x	0
y	0
z	0
Occupancy	1

Structural parameters for MPS: space group *I4*, $a = b = 5.5754(9)$ Å, $c = 8.170(2)$ Å, and $V = 254$ Å³. $\chi^2 = 3.426$, $wR_p = 7.11$ %, and $R_p = 5.20$ %.

^a Only the position of Pt within the crystal structure could be ascertained from the sample due to poor crystallinity and trace impurities (see text).

Table 5. Calculated ZORA ¹⁹⁵ Pt isotropic shielding and experimental chemical shifts for Magnus' Green Salt and reagents.

Label	System	Pt Label ^a	Exper. δ_{iso} (ppm) ^b	Calculated: PBE0/QZ4P/TZP		
				σ_{iso} (ppm)		$\Delta\sigma_{\text{iso}}$ ^c (ppm)
				Scalar (SC)	Spin-Orbit (SO)	SO-SC
A	$[(\text{Pt}(\text{NH}_3)_4)_3\text{Cl}_8]^{2-}$	2	-2507(10)	470	4034	3563
B ^d	$[\text{K}_8(\text{PtCl}_4)_3]^{2+}$	2	-1510(60)	-1401	2231	3632
B' ^e	$[\text{K}_8(\text{PtCl}_4)_3]^{2+}$	2		-690	2845	3536
C	MGS $\text{Pt}(\text{NH}_3)_4^{2+}$	3	-2208(6)	-221	3515	3740
D	PtCl_4^{2-}	2	-970(6)	-1547	2247	3802

^a Label of the Pt center, see Figure 11. ^b δ_{iso} values of A, C, D were taken from MAS experiments, and δ_{iso} values of B/B' from WURST-CPMG experiments. ^c $\Delta\sigma_{\text{iso}} = \sigma_{\text{iso}}(\text{SO}) - \sigma_{\text{iso}}(\text{SC})$. ^d Optimized structure, Pt-Cl: 2.337 Å. ^e X-ray crystal structure, Pt-Cl: 2.309 Å

Table 6. ^{195}Pt NMR comparison of Magnus' Green Salt and reagents.

X vs. Y ^a	Exp. $\Delta\delta_{\text{iso}}$ (X-Y) (ppm) ^b	SC $\Delta\sigma_{\text{iso}}$ (Y-X) (ppm) ^c	SO $\Delta\sigma_{\text{iso}}$ (Y-X) (ppm) ^c
A vs. B	-997	-1871	-1802
A vs. B'		-1161	-1188
C vs. D	-1238	-1330	-1269
A vs. C	-299	-695	-519
B vs. D	-540	-154	15
B' vs. D		-865	-599

^a Labels according to Table 5. ^b $\Delta\delta_{\text{iso}}(\text{X-Y}) = \delta_{\text{iso}}(\text{X}) - \delta_{\text{iso}}(\text{Y})$. ^c $\Delta\sigma_{\text{iso}}(\text{Y-X}) = \sigma_{\text{iso}}(\text{Y}) - \sigma_{\text{iso}}(\text{X})$. Note that the order of subtraction (i.e., X-Y vs. Y-X) changes between columns due to the conventions (δ vs. σ) of the chemical shift and magnetic shielding scales.

Table 7. Calculated scalar and spin-orbit ZORA ^{195}Pt shielding tensors for MGS and reagents.^{a,b}

		ZORA Calculations					Experimental	
		σ_{11}	σ_{22}	σ_{33}	Ω	κ	Ω	κ
A	SC	-3893	2590	2714	6483	-0.98	7200(50)	-0.995(5)
	SO	-462	6228	6335	6797	-0.97		
B	SC	-8358	2077	2079	10435	-1.00	10420(100)	-0.97(1)
	SO	-4438	5564	5568	10006	-1.00		
B' ^c	SC	-6939	2432	2436	9370	-1.00	10420(100)	-0.97(1)
	SO	-3121	5826	5831	8952	-1.00		
C	SC	-4930	2133	2133	7063	-1.00	7560(30)	-1.00(1)
	SO	-1265	5909	5909	7174	-1.00		
D ^c	SC	-8519	1939	1939	10458	-1.00	10575(50)	-1.00(1)
	SO	-4571	5666	5666	10237	-1.00		

^a σ is given in ppm, κ is dimensionless. ^b Labeling scheme according to Table 5. ^c See Figure 12 for graphical representation.

Table 8. Magnetic shielding analysis (in ppm) in terms of LMOs for Magnus' Green Salt and reagents. ^a

	$[(\text{Pt}(\text{NH}_3)_4)_3\text{Cl}_8]^{2-}$	$[\text{K}_8(\text{PtCl}_4)_3]^{2+}$ ^b	MGS $\text{Pt}(\text{NH}_3)_4^{2+}$	MGS PtCl_4^{2-}	$\Delta \text{Pt}(\text{NH}_3)_4^{2+}$ ^c	$\Delta \text{PtCl}_4^{2-}$ ^c
Σ Pt	4511	3202	4000	2651	-511	-551
Σ Unocc.	-481	-331	-391	-351	90	-20
Σ Counterion	9	-9	n/a	n/a	n/a	n/a
Σ Other Pt's	-6	-16	-91	-46	n/a	n/a
Σ Pt CR	11598	11985	11583	11998	-15	13
$\Sigma \sigma(\text{Pt-ligand})$	-708	-856	-583	-796	125	60
Σ ligand	56	-9	113	-16	57	-7
Pt d_{xy}	-3649	-4676	-4016	-5101	-367	-425
Pt d_{xz}, d_{yz}	-2811	-3151	-3359	-3639	-548	-488
Pt d_{z^2}	25	-91	263	206	238	297
Σ Pt LP	-6435	-7919	-7112	-8534	-677	-615
σ_{iso}	4034	2845	3518	2254	-516	-591

^a Spin-orbit ZORA computations, and breakdown in terms of "natural" localized molecular orbitals, obtained from the NBO program for the corresponding scalar relativistic system (see Experimental section). Separate contributions for all the Pt units, counterion, and variational spin-orbit term (Σ Unocc.) together with contributions from core (CR), Pt-ligand σ bonds, ligand and Pt 5d lone-pair (LP) LMOs for the central Pt unit of the cluster (Figure 11) is given. The first three columns refer to Pt(2) of the corresponding cluster in Figure 11, the fourth column refers to Pt(3). All values are listed in ppm. ^b X-ray crystal structure, Pt-Cl: 2.309 Å. Optimized geometries used otherwise.

^c Calculated: difference between MGS and reference. Experimental: difference between reference and MGS.

Figure Captions.

Scheme 1. Schematic representations of (a) K_2PtCl_4 , (b) $\text{Pt}(\text{NH}_3)_4\text{Cl}_2 \cdot \text{H}_2\text{O}$, (c) Magnus' Green Salt ($[\text{Pt}(\text{NH}_3)_4][\text{PtCl}_4]$) and (d) Magnus' Pink Salt ($[\text{Pt}(\text{NH}_3)_4][\text{PtCl}_4]$). Depictions are based on experimentally-determined crystal structures, except for Magnus' Pink Salt, which has been postulated to adopt the shown arrangement, but has no reported crystal structure to date.

Figure 1. ^{195}Pt static WURST-CPMG NMR spectra of (a) $\text{Pt}(\text{NH}_3)_4\text{Cl}_2 \cdot \text{H}_2\text{O}$, (b) K_2PtCl_4 , (c) Magnus' Green Salt, and ^1H - ^{195}Pt static BRAIN-CP/WCPMG NMR spectra of (d) Magnus' Pink Salt, (e) $\text{Pt}(\text{NH}_3)_4\text{Cl}_2 \cdot \text{H}_2\text{O}$, and (f) MGS. Asterisks (*) denote interference from local FM radio stations. Dashed lines indicate the high frequency edge (δ_{11}) of the powder patterns of the starting reagents. The (d) spectrum is shown at the bottom of each column for comparison to the spectra above (see text for details).

Figure 2. Individual static Hahn-echo ^{195}Pt NMR spectra (i.e., single sub-spectra excited by a single rectangular pulse) of (a) $\text{Pt}(\text{NH}_3)_4\text{Cl}_2 \cdot \text{H}_2\text{O}$, (b) WURST-CPMG spectrum of K_2PtCl_4 co-added in the time domain,⁵⁰ (c) Hahn-echo spectrum of MGS. ^1H - ^{195}Pt CP-echo NMR spectra of MGS using a (d) 16 ms contact time and (e) 3 ms contact time, as well as CP-echo NMR spectra of MPS using a (f) 15 ms contact time and (g) 3 ms contact time.

Figure 3. Individual ^1H - ^{195}Pt CP-echo NMR spectra (i.e., single sub-spectra excited by a single rectangular pulse) of MPS. (a) A two-site simulation along with experimental spectra utilizing a contact time of (i) 3 ms and (ii) 15 ms. (b) Experimental spectrum (contact time of 3 ms) along with simulated spectra (dashed lines) accounting for two unique Pt sites in MPS along with $\text{Pt}(\text{NH}_3)_4\text{Cl}_2 \cdot \text{H}_2\text{O}$ and MGS impurities at

relative integrated intensities of (i) 40% and (ii) 10 %.

Figure 4. ^{195}Pt MAS NMR spectra of (a) MGS and (b, c) MPS. The MGS spectrum shown in (a) was acquired using a recycle delay of 40 s, while a recycle delay of 90 s and 8 s were used to acquire the MPS spectra depicted in (b) and (c), respectively.

Figure 5. ^{14}N static NMR spectra (bottom traces) and simulations (top traces) of (a) $\text{Pt}(\text{NH}_3)_4\text{Cl}_2 \cdot \text{H}_2\text{O}$, (b) MGS, and (c) MPS. Spectra on the left were acquired with direct-excitation WURST-QCPMG experiments, spectra on the right were acquired using ^1H - ^{14}N BRAIN-CP/WCPMG experiments.

Figure 6. Static WURST-QCPMG ^{35}Cl NMR spectra acquired at 21.1 T (bottom traces) and simulations (top traces) of (a) K_2PtCl_4 , (b) $\text{Pt}(\text{NH}_3)_4\text{Cl}_2 \cdot \text{H}_2\text{O}$ (with Hahn-echo experiment inset), (c) MGS, and (d) MPS.

Figure 7. Powder X-ray diffraction patterns of square-planar Pt complexes. Two separate batches of MPS product were studied in order to assess the reliability of the synthesis.

Figure 8. Le Bail fit for pXRD data of MPS using the parameters described in Table 4.

Figure 9. Visualization of the electron density map obtained via the refinement of MPS powder X-ray diffraction data. Yellow denotes Pt atoms, red denotes localized areas of electron density associated with Pt ligands.

Figure 10. Proposed structural model of MPS, based on SSNMR and pXRD data. Yellow denotes Pt atoms, blue denotes electron density assigned to -NH_3 ligands, and green denotes electron density assigned to -Cl ligands.

Figure 11. Molecular clusters used in the NMR calculations. The numbers listed correspond to calculated (experimental) geometric parameters.

Figure 12. Graphical representations of the direction-dependent platinum shielding in (a) MGS and (b) K_2PtCl_4 . Blue and orange indicate positive and negative shielding, respectively. Polar plots of the shielding tensors are scaled by 0.025 pm/ppm.

Figure 13. If low-energy unoccupied orbitals can overlap with a ‘magnetic field rotated’ Pt 5d orbital, a deshielding contribution is obtained in the MS tensor component parallel to the field. This causes deshielding in 6-coordinate Pt(IV) vs. 4-coordinate Pt(II), as shown in Reference 68. In MGS, similar orbital interactions create deshielding contributions from the Pt 5d nonbonding orbitals in all principal MS tensor components relative to the 4-coordinate Pt(II) starting reagents.

References

- (1) Williams, J. A. G. In *Photochemistry and Photophysics of Coordination Compounds II*; Balzani, V., Campagna, S., Eds.; Springer DE: Berlin, 2007; Vol. 281, pp 205.
- (2) Qin, Z. Q.; Jennings, M. C.; Puddephatt, R. J. *Inorg. Chem.* **2003**, *42*, 1956.
- (3) Mdleleni, M. M.; Bridgewater, J. S.; Watts, R. J.; Ford, P. C. *Inorg. Chem.* **1995**, *34*, 2334.
- (4) Hissler, M.; Connick, W. B.; Geiger, D. K.; McGarrah, J. E.; Lipa, D.; Lachicotte, R. J.; Eisenberg, R. *Inorg. Chem.* **2000**, *39*, 447.
- (5) Connick, W. B.; Henling, L. M.; Marsh, R. E.; Gray, H. B. *Inorg. Chem.* **1996**, *35*, 6261.
- (6) Brooks, J.; Babayan, Y.; Lamansky, S.; Djurovich, P. I.; Tsyba, I.; Bau, R.; Thompson, M. E. *Inorg. Chem.* **2002**, *41*, 3055.
- (7) Jain, V. K.; Jain, L. *Coordin. Chem. Rev.* **2010**, *254*, 2848.
- (8) Eryazici, I.; Moorefield, C. N.; Newkome, G. R. *Chem. Rev.* **2008**, *108*, 1834.
- (9) Reedijk, J. *Chem. Commun.* **1996**, 801.
- (10) Sundquist, W. I.; Lippard, S. J. *Coordin. Chem. Rev.* **1990**, *100*, 293.
- (11) Knipp, M. *Curr. Med. Chem.* **2009**, *16*, 522.
- (12) Momekov, G.; Momekova, D. *Expert Opin. Ther. Pat.* **2006**, *16*, 1383.
- (13) Todd, R. C.; Lippard, S. J. *Metallomics* **2009**, *1*, 280.
- (14) Lecointe, P.; Macquet, J. P.; Butour, J. L.; Paoletti, C. *Mutat. Res.* **1977**, *48*, 139.
- (15) Lippert, B. *Prog. Inorg. Chem.* **1989**, *37*, 1.
- (16) Vanbeusichem, M.; Farrell, N. *Inorg. Chem.* **1992**, *31*, 634.
- (17) Doerrler, L. H. *Dalton Trans.* **2010**, *39*, 3543.

- (18) Caseri, W. *Platinum Met. Rev.* **2004**, *48*, 91.
- (19) Roundhill, D. M.; Gray, H. B.; Che, C. M. *Acc. Chem. Res.* **1989**, *22*, 55.
- (20) Miller, J. S. *Inorg. Chem.* **1976**, *15*, 2357.
- (21) Miller, J. S.; Epstein, A. J. *Prog. Inorg. Chem.* **1976**, *20*, 1.
- (22) Pyykko, P. *Chem. Rev.* **1997**, *97*, 597.
- (23) Pyykko, P. *Angew. Chem. Int. Edit.* **2004**, *43*, 4412.
- (24) Jiang, Y.; Alvarez, S.; Hoffmann, R. *Inorg. Chem.* **1985**, *24*, 749.
- (25) Scherbaum, F.; Grohmann, A.; Huber, B.; Kruger, C.; Schmidbaur, H. *Angew. Chem. Int. Edit.* **1988**, *27*, 1544.
- (26) Magnus, G. *Pogg. Ann.* **1828**, *11*, 242.
- (27) Atoji, M.; Richardson, J. W.; Rundle, R. E. *J. Am. Chem. Soc.* **1957**, *79*, 3017.
- (28) Interrante, L.; Messmer, R. P. *Inorg. Chem.* **1971**, *10*, 1174.
- (29) Musselman, R. L. *Inorg. Chim. Acta* **2008**, *361*, 820.
- (30) Breimi, J.; Brovelli, D.; Caseri, W.; Hahner, G.; Smith, P.; Tervoort, T. *Chem. Mat.* **1999**, *11*, 977.
- (31) Breimi, J.; Gramlich, V.; Caseri, W.; Smith, P. *Inorg. Chim. Acta* **2001**, *322*, 23.
- (32) Hertel, E.; Schneider, K. *Z. Anorg. Allg. Chem.* **1931**, *202*, 77.
- (33) Jorgensen, S. M.; Sorensen, S. P. L. *Z. Anorg. Allg. Chem.* **1906**, *48*, 441.
- (34) Still, B. M.; Kumar, P. G. A.; Aldrich-Wright, J. R.; Price, W. S. *Chem. Soc. Rev.* **2007**, *36*, 665.
- (35) Priqueler, J. R. L.; Butler, I. S.; Rochon, F. D. *Appl. Spectrosc. Rev.* **2006**, *41*, 185.
- (36) Truflandier, L. A.; Autschbach, J. *J. Am. Chem. Soc.* **2010**, *132*, 3472.
- (37) Truflandier, L. A.; Sutter, K.; Autschbach, J. *Inorg. Chem.* **2011**, *50*, 1723.

- (38) Sutter, K.; Truflandier, L. A.; Autschbach, J. *ChemPhysChem* **2011**, *12*, 1448.
- (39) Pregosin, P. S. In *Annual Reports on NMR Spectroscopy*; Webb, G. A., Ed.; Academic Press: New York, 1986; Vol. 17, p 356.
- (40) Goodfellow, R. J. In *Multinuclear NMR*; First ed.; Mason, J., Ed.; Plenum Press: New York, 1987, p 639.
- (41) Lucier, B. E. G.; Reidel, A. R.; Schurko, R. W. *Can. J. Chem.* **2011**, *89*, 919.
- (42) O'Dell, L. A.; Schurko, R. W. *Chem. Phys. Lett.* **2008**, *464*, 97.
- (43) Tang, J. A.; O'Dell, L. A.; Aguiar, P. M.; Lucier, B. E. G.; Sakellariou, D.; Schurko, R. W. *Chem. Phys. Lett.* **2008**, *466*, 227.
- (44) O'Dell, L. A.; Rossini, A. J.; Schurko, R. W. *Chem. Phys. Lett.* **2009**, *468*, 330.
- (45) Kupce, E.; Freeman, R. *J. Magn. Reson., Ser. A* **1995**, *115*, 273.
- (46) Bhattacharyya, R.; Frydman, L. *J. Chem. Phys.* **2007**, *127*, 194503/1.
- (47) Larsen, F. H.; Jakobsen, H. J.; Ellis, P. D.; Nielsen, N. C. *J. Phys. Chem. A* **1997**, *101*, 8597.
- (48) Harris, K. J.; Lupulescu, A.; Lucier, B. E. G.; Frydman, L.; Schurko, R. W. *J. Mag. Reson.* **2012**, *224*, 38.
- (49) Hudson, Z. M.; Sun, C.; Harris, K. J.; Lucier, B. E. G.; Schurko, R. W.; Wang, S. N. *Inorg. Chem.* **2011**, *50*, 3447.
- (50) MacGregor, A. W.; O'Dell, L. A.; Schurko, R. W. *J. Mag. Reson.* **2011**, *208*, 103.
- (51) Honda, K.; Chiba, K.; Tsuchida, E.; Frank, A. J. *J. Mater. Sci.* **1989**, *24*, 4004.
- (52) Palkin, V. A.; Kuzina, T. A.; Kuzmina, N. N.; Shchelokov, R. N. *J. Anal. Chem.-USSR* **1980**, *25*, 1291.

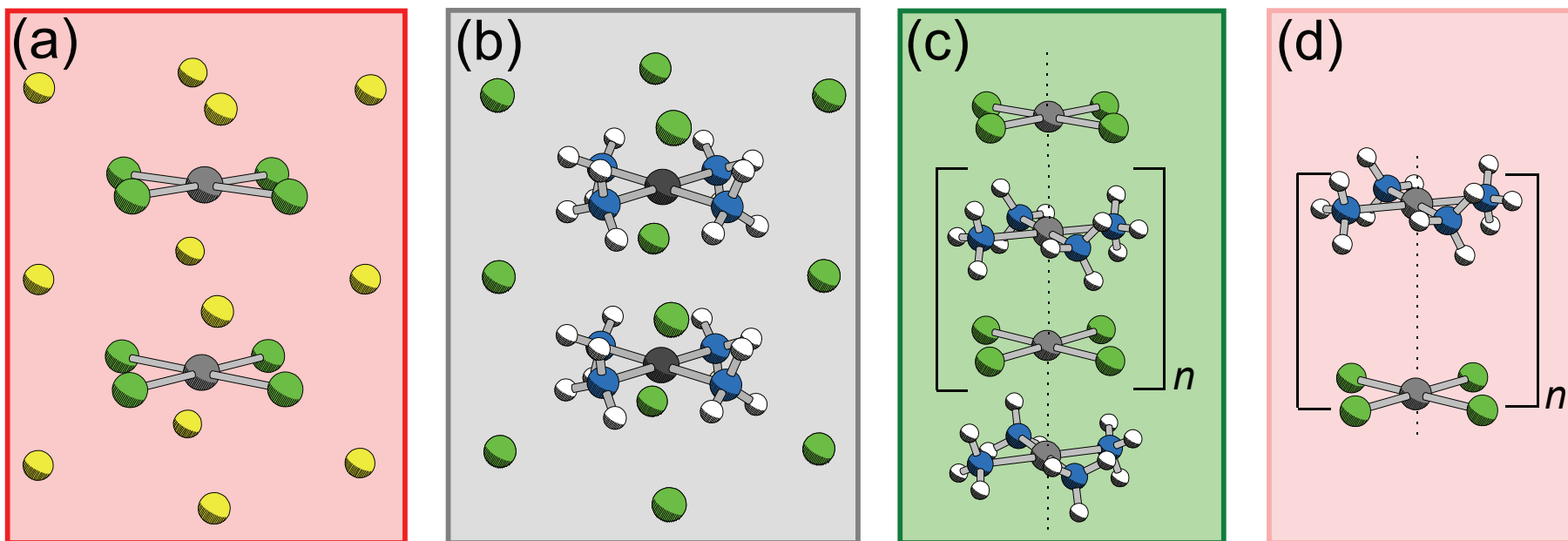
- (53) Yamada, S. *J. Am. Chem. Soc.* **1951**, *73*, 1579.
- (54) Massiot, D.; Farnan, I.; Gautier, N.; Trumeau, D.; Florian, P.; Grandinetti, P. J. *J. Chim. Phys. PCB* **1995**, *92*, 1847.
- (55) Medek, A.; Frydman, V.; Frydman, L. *J. Phys. Chem. A* **1999**, *103*, 4830.
- (56) Tang, J. A.; Masuda, J. D.; Boyle, T. J.; Schurko, R. W. *ChemPhysChem* **2006**, *7*, 117.
- (57) Lipton, A. S.; Wright, T. A.; Bowman, M. K.; Reger, D. L.; Ellis, P. D. *J. Am. Chem. Soc.* **2002**, *124*, 5850.
- (58) O'Dell, L. A.; Ratcliffe, C. I. *Chem. Commun.* **2010**, *46*, 6774.
- (59) Eichele, K., WSolids1, version 1.20.15, Universität of Tübingen, Tübingen, Germany, 2011.
- (60) Massiot, D.; Fayon, F.; Capron, M.; King, I.; Le Calve, S.; Alonso, B.; Durand, J.-O.; Bujoli, B.; Gan, Z.; Hoatson, G. *Magn. Reson. Chem.* **2002**, *40*, 70.
- (61) ADF2011.01, SCM, Vrije Universiteit, Amsterdam, The Netherlands,
- (62) Velde, G. T.; Bickelhaupt, F. M.; Baerends, E. J.; Guerra, C. F.; Van Gisbergen, S. J. A.; Snijders, J. G.; Ziegler, T. *J. Comput. Chem.* **2001**, *22*, 931.
- (63) Perdew, J. P.; Burke, K.; Ernzerhof, M. *Phys. Rev. Lett.* **1996**, *77*, 3865.
- (64) Perdew, J. P.; Burke, K.; Ernzerhof, M. *Phys. Rev. Lett.* **1997**, *78*, 1396.
- (65) Ernzerhof, M.; Scuseria, G. E. *J. Chem. Phys.* **1999**, *110*, 5029.
- (66) Adamo, C.; Barone, V. *J. Chem. Phys.* **1999**, *110*, 6158.
- (67) Sterzel, M.; Autschbach, J. *Inorg. Chem.* **2006**, *45*, 3316.
- (68) Autschbach, J.; Zheng, S. H. *Magn. Reson. Chem.* **2008**, *46*, S45.
- (69) Davis, J. C.; Buhl, M.; Koch, K. R. *Journal of Chemical Theory and Computation* **2012**, *8*, 1344.

- (70) van Lenthe, E.; Baerends, E. J.; Snijders, J. G. *J. Chem. Phys.* **1993**, *99*, 4597.
- (71) Wolff, S. K.; Ziegler, T.; van Lenthe, E.; Baerends, E. J. *J. Chem. Phys.* **1999**, *110*, 7689.
- (72) Autschbach, J.; Zurek, E. *J. Phys. Chem. A* **2003**, *107*, 4967.
- (73) Glendening, E. D.; Badenhop, J. K.; Reed, A. E.; Carpenter, J. E.; Bohmann, J. A.; Morales, C. M.; Weinhold, F., NBO 5.0, Theoretical Chemistry Institute, University of Wisconsin, Madison, 2001.
- (74) Weinhold, F. In *Encyclopedia of Computational Chemistry*; von Ragué Schleyer, P., Ed.; John Wiley & Sons: Chichester, 1998, pp 1792.
- (75) Autschbach, J. *J. Chem. Phys.* **2008**, *128*.
- (76) Cox, E. G. *J. Chem. Soc.* **1932**, 1912.
- (77) Mais, R. H. B.; Wood, A. M.; Owston, P. G. *Acta Crystallogr. B* **1972**, *B 28*, 393.
- (78) Baroni, S.; de Gironcoli, S.; Corso, A. D.; Giannozzi, P., PWscf. Plane-Wave Self-Consistent Field, 2009.
- (79) Giannozzi, P.; Baroni, S.; Bonini, N.; Calandra, M.; Car, R.; Cavazzoni, C.; Ceresoli, D.; Chiarotti, G. L.; Cococcioni, M.; Dabo, I.; Dal Corso, A.; de Gironcoli, S.; Fabris, S.; Fratesi, G.; Gebauer, R.; Gerstmann, U.; Gougoussis, C.; Kokalj, A.; Lazzeri, M.; Martin-Samos, L.; Marzari, N.; Mauri, F.; Mazzarello, R.; Paolini, S.; Pasquarello, A.; Paulatto, L.; Sbraccia, C.; Scandolo, S.; Sclauzero, G.; Seitsonen, A. P.; Smogunov, A.; Umari, P.; Wentzcovitch, R. M. *J. Phys. - Condens. Mat.* **2009**, *21*, 395502.
- (80) Vanderbilt, D. *Phys. Rev. B* **1990**, *41*, 7892.
- (81) Morosin, B.; Fallon, P.; Valentine, J. S. *Acta Crystallogr. B* **1975**, *31*, 2220.
- (82) Rietveld, H. *J. Appl. Crystallogr.* **1969**, *2*, 65.
- (83) Larson, A. C.; Von Dreele, R. B. "General Structure Analysis System (GSAS)," Los Alamos

National Laboratory Report LA-UR-86-748, 2000.

- (84) Toby, B. H. *J. Appl. Crystallogr.* **2001**, *34*, 210.
- (85) Hammersley, A. P.; Svensson, S. O.; Hanfland, M.; Fitch, A. N.; Hausermann, D. *High Pressure Res.* **1996**, *14*, 235.
- (86) Favre-Nicolin, V.; Cerny, R. *J. Appl. Crystallogr.* **2002**, *35*, 734.
- (87) Tang, J. A.; Kogut, E.; Norton, D.; Lough, A. J.; McGarvey, B. R.; Fekl, U.; Schurko, R. W. *J. Phys. Chem. B* **2009**, *113*, 3298.
- (88) Sparks, S. W.; Ellis, P. D. *J. Am. Chem. Soc.* **1986**, *108*, 3215.
- (89) Keller, H. J.; Rupp, H. H. *Z. Naturforsch., A: Phys. Sci.* **1970**, *A 25*, 312.
- (90) Keller, H. J.; Rupp, H. H. *Z. Naturforsch., A: Phys. Sci.* **1971**, *A 26*, 785.
- (91) Briand, G. G.; Smith, A. D.; Schatte, G.; Rossini, A. J.; Schurko, R. W. *Inorg. Chem.* **2007**, *46*, 8625.
- (92) O'Dell, L. A.; Schurko, R. W.; Harris, K. J.; Autschbach, J.; Ratcliffe, C. I. *J. Am. Chem. Soc.* **2011**, *133*, 527.
- (93) O'Dell, L. A. *Prog. Nucl. Magn. Reson. Spectrosc.* **2011**, *59*, 295.
- (94) O'Dell, L. A.; Schurko, R. W. *J. Am. Chem. Soc.* **2009**, *131*, 6658.
- (95) O'Dell, L. A.; Schurko, R. W. *Phys. Chem. Chem. Phys.* **2009**, *11*, 7069.
- (96) Penner, G. H.; Webber, R.; O'Dell, L. A. *Can. J. Chem.* **2011**, *89*, 1036.
- (97) O'Dell, L. A.; Ratcliffe, C. I.; Kong, X. Q.; Wu, G. *J. Phys. Chem. A* **2012**, *116*, 1008.
- (98) Bryce, D. L.; Sward, G. D.; Adiga, S. *J. Am. Chem. Soc.* **2006**, *128*, 2121.
- (99) Chapman, R. P.; Bryce, D. L. *Phys. Chem. Chem. Phys.* **2007**, *9*, 6219.

- (100) Bryce, D. L.; Bultz, E. B. *Chem. Eur. J* **2007**, *13*, 4786.
- (101) Hamaed, H.; Pawlowski, J. M.; Cooper, B. F. T.; Fu, R. Q.; Eichhorn, S. H.; Schurko, R. W. *J. Am. Chem. Soc.* **2008**, *130*, 11056.
- (102) Gordon, P. G.; Brouwer, D. H.; Ripmeester, J. A. *J. Phys. Chem. A* **2008**, *112*, 12527.
- (103) Gordon, P. G.; Brouwer, D. H.; Ripmeester, J. A. *ChemPhysChem* **2010**, *11*, 260.
- (104) Chapman, R. P.; Widdifield, C. M.; Bryce, D. L. *Prog. Nucl. Magn. Reson. Spectrosc.* **2009**, *55*, 215.
- (105) Chapman, R. P.; Bryce, D. L. *Phys. Chem. Chem. Phys.* **2009**, *11*, 6987.
- (106) Rossini, A. J.; Mills, R. W.; Briscoe, G. A.; Norton, E. L.; Geier, S. J.; Hung, I.; Zheng, S.; Autschbach, J.; Schurko, R. W. *J. Am. Chem. Soc.* **2009**, *131*, 3317.
- (107) Hung, I.; Shetty, K.; Ellis, P. D.; Brey, W. W.; Gan, Z. H. *Solid State Nucl. Magn. Reson.* **2009**, *36*, 159.
- (108) Perras, F. A.; Bryce, D. L. *J. Mag. Reson.* **2011**, *213*, 82.
- (109) Johnston, K. E.; O'Keefe, C. A.; Gauvin, R. M.; Trébosch, J.; Delevoye, L.; Amoureux, J.-P.; Popoff, N.; Taoufik, M.; Oudatchin, K.; Schurko, R. W. *Chem. Eur. J* **2013**, *In press*, DOI: 10.1002/chem.201301268.
- (110) Zurek, E.; Pickard, C. J.; Autschbach, J. *J. Phys. Chem. A* **2009**, *113*, 4117.
- (111) Hansen, A. E.; Bouman, T. D. *J. Chem. Phys.* **1989**, *91*, 3552.
- (112) Widdifield, C. M.; Schurko, R. W. *Concept. Magnetic Res. A* **2009**, *34A*, 91.



Scheme 1. Schematic representations of (a) K_2PtCl_4 , (b) $\text{Pt}(\text{NH}_3)_4\text{Cl}_2 \cdot \text{H}_2\text{O}$, (c) Magnus' Green Salt ($[\text{Pt}(\text{NH}_3)_4][\text{PtCl}_4]$) and (d) Magnus' Pink Salt ($[\text{Pt}(\text{NH}_3)_4][\text{PtCl}_4]$). Depictions are based on experimentally-determined crystal structures, except for Magnus' Pink Salt, which has been postulated to adopt the shown arrangement, but has no reported crystal structure to date.

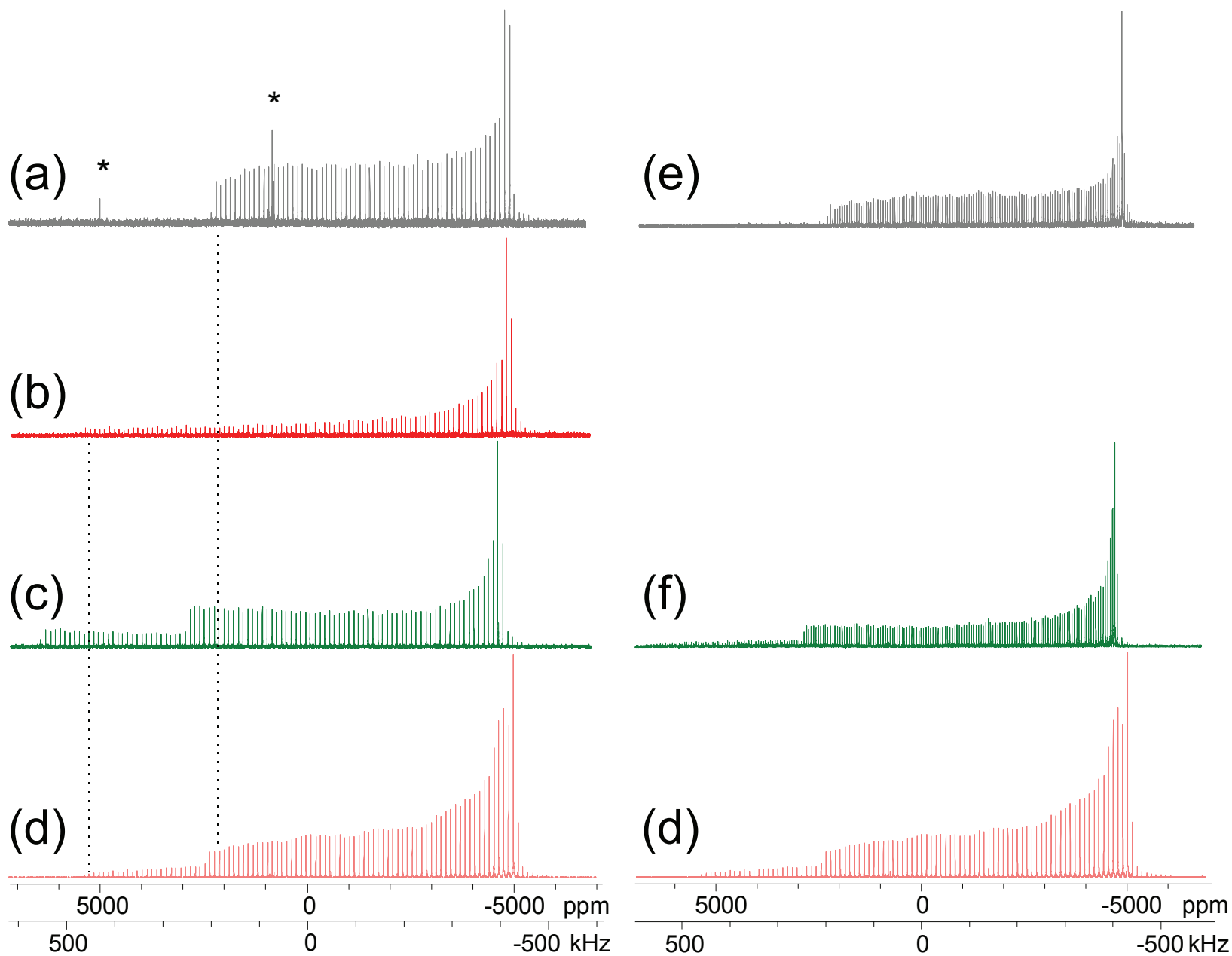


Figure 1. ^{195}Pt static WURST-CPMG NMR spectra of (a) $\text{Pt}(\text{NH}_3)_4\text{Cl}_2 \cdot \text{H}_2\text{O}$, (b) K_2PtCl_4 , (c) Magnus' Green Salt, and ^1H - ^{195}Pt static BRAIN-CP/WCPMG NMR spectra of (d) Magnus' Pink Salt, (e) $\text{Pt}(\text{NH}_3)_4\text{Cl}_2 \cdot \text{H}_2\text{O}$, and (f) MGS. Asterisks (*) denote interference from local FM radio stations. Dashed lines indicate the high frequency edge (δ_{11}) of the powder patterns of the starting reagents. The (d) spectrum is shown at the bottom of each column for comparison to the spectra above (see text for details).

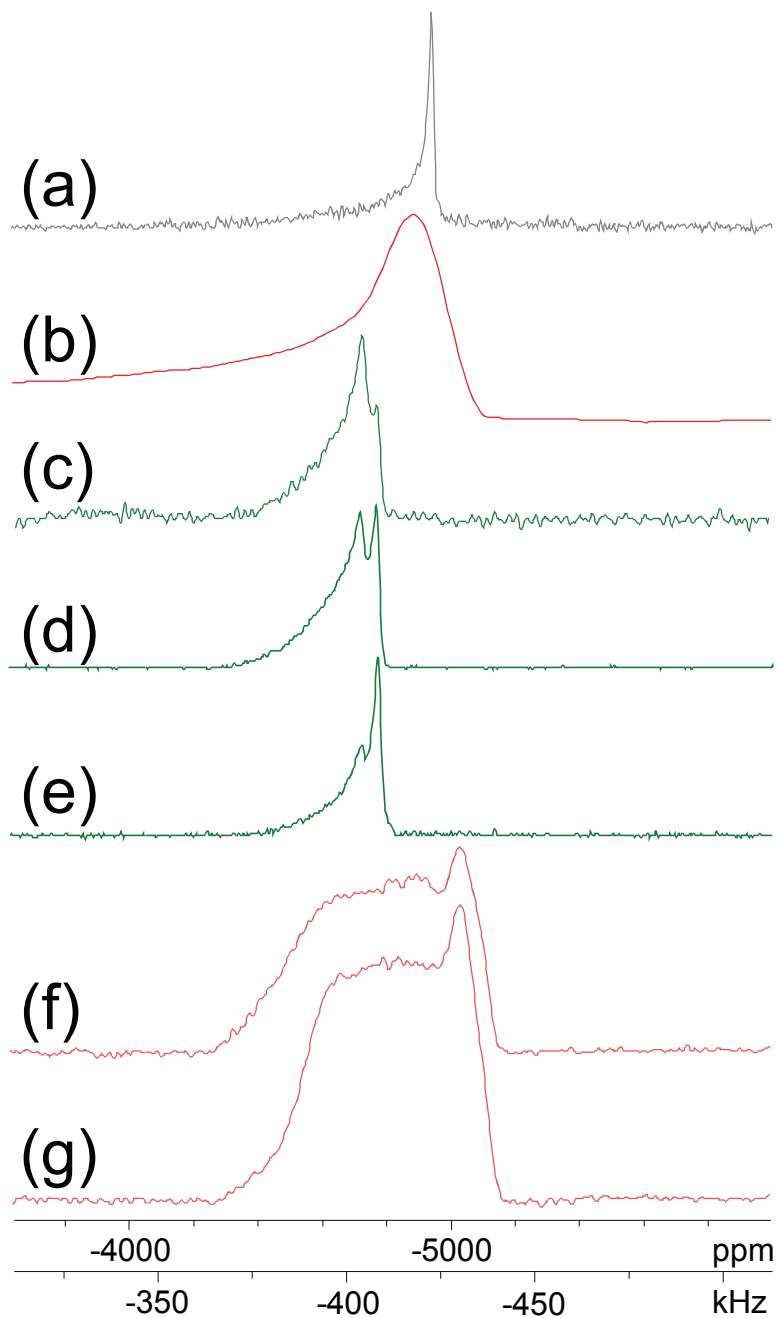


Figure 2. Individual static Hahn-echo ^{195}Pt NMR spectra (i.e., single sub-spectra excited by a single rectangular pulse) of (a) $\text{Pt}(\text{NH}_3)_4\text{Cl}_2 \cdot \text{H}_2\text{O}$, (b) WURST-CPMG spectrum of K_2PtCl_4 co-added in the time domain,⁵⁰ (c) Hahn-echo spectrum of MGS. ^1H - ^{195}Pt CP-echo NMR spectra of MGS using a (d) 16 ms contact time and (e) 3 ms contact time, as well as CP-echo NMR spectra of MPS using a (f) 15 ms contact time and (g) 3 ms contact time.

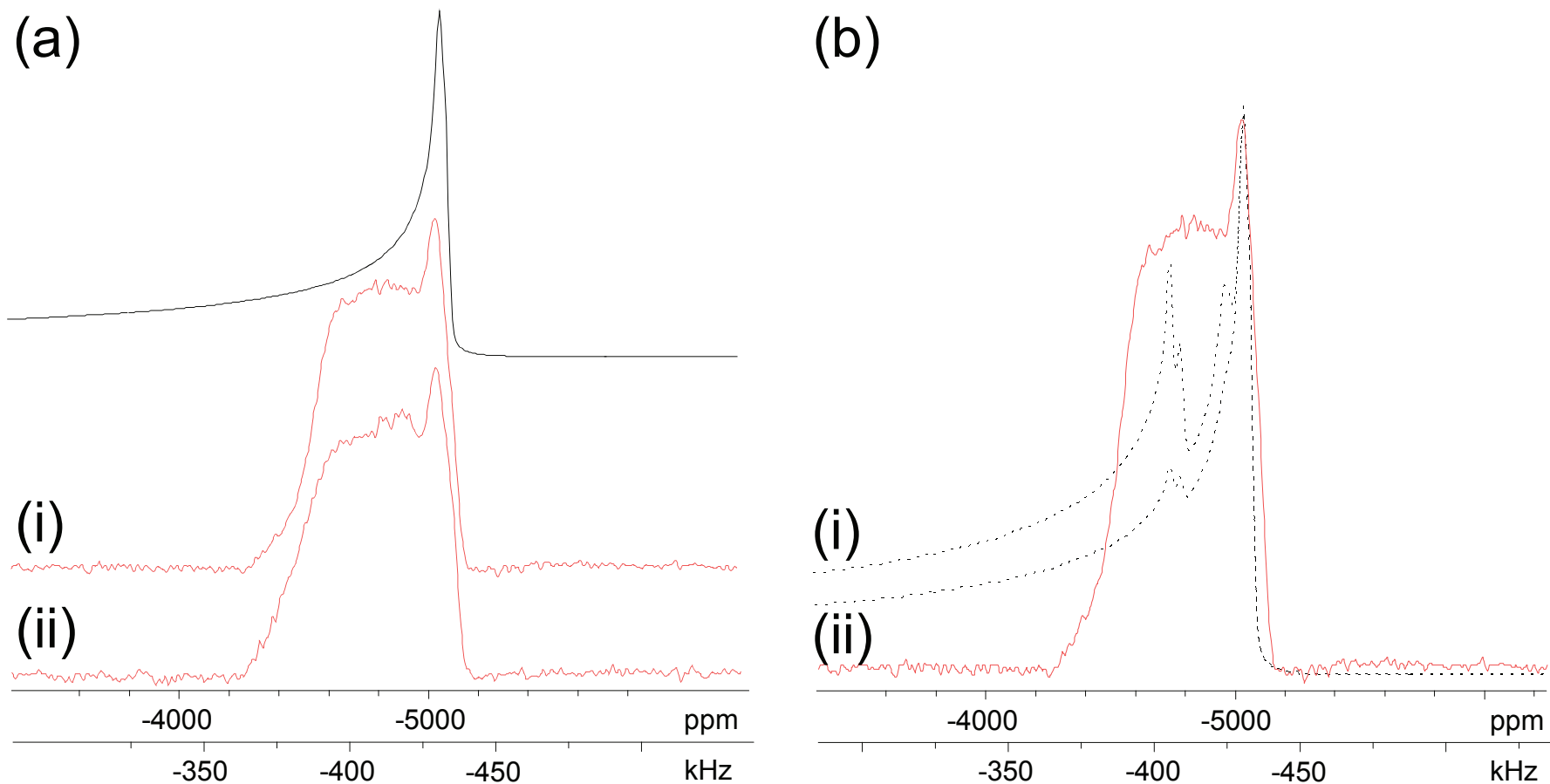


Figure 3. Individual ^1H - ^{195}Pt CP-echo NMR spectra (i.e., single sub-spectra excited by a single rectangular pulse) of MPS. (a) A two-site simulation along with experimental spectra utilizing a contact time of (i) 3 ms and (ii) 15 ms. (b) Experimental spectrum (contact time of 3 ms) along with simulated spectra (dashed lines) accounting for two unique Pt sites in MPS along with $\text{Pt}(\text{NH}_3)_4\text{Cl}_2 \cdot \text{H}_2\text{O}$ and MGS impurities at relative integrated intensities of (i) 40% and (ii) 10 %.

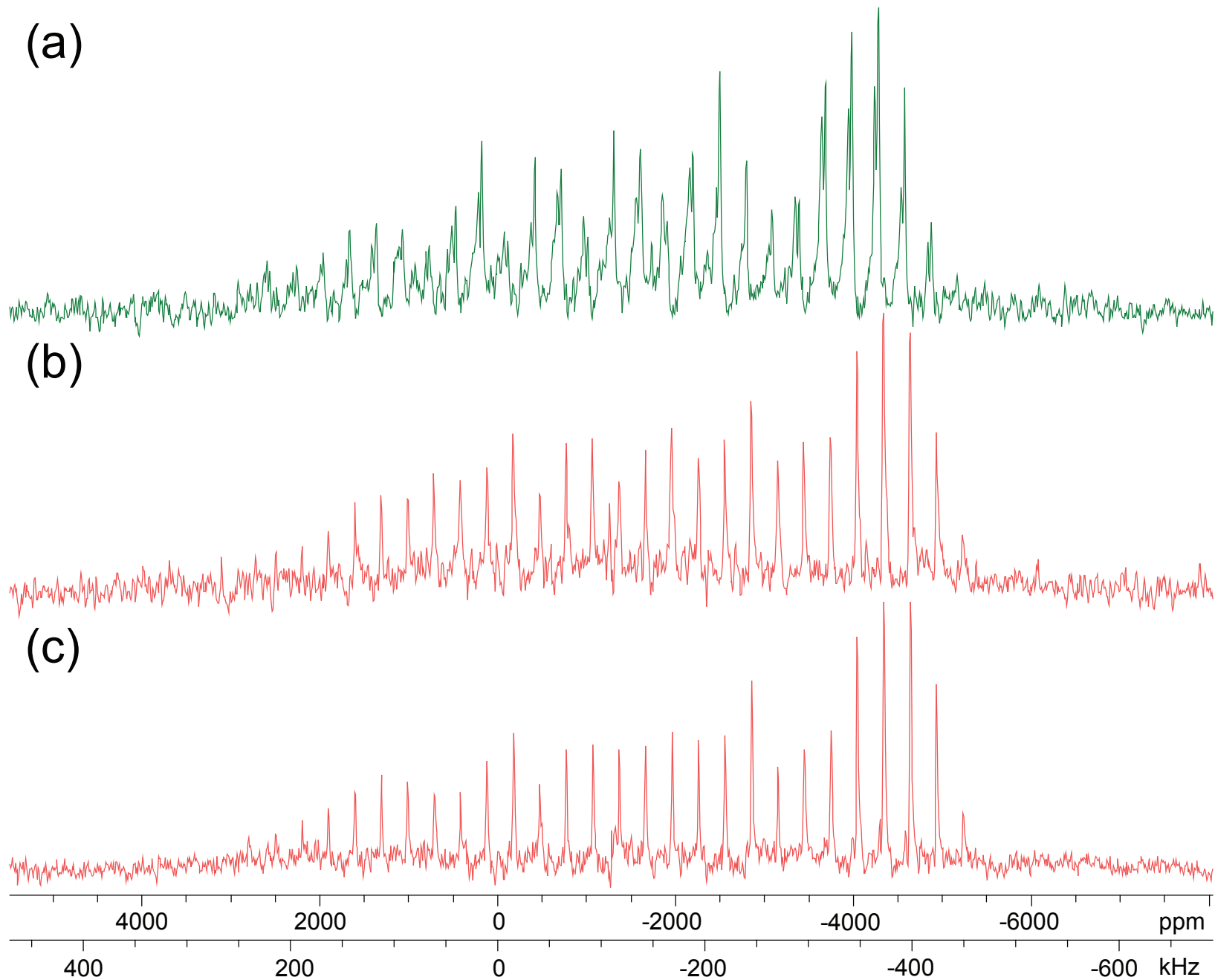


Figure 4. ^{195}Pt MAS NMR spectra of (a) MGS and (b, c) MPS. The MGS spectrum shown in (a) was acquired using a recycle delay of 40 s, while a recycle delay of 90 s and 8 s were used to acquire the MPS spectra depicted in (b) and (c), respectively.

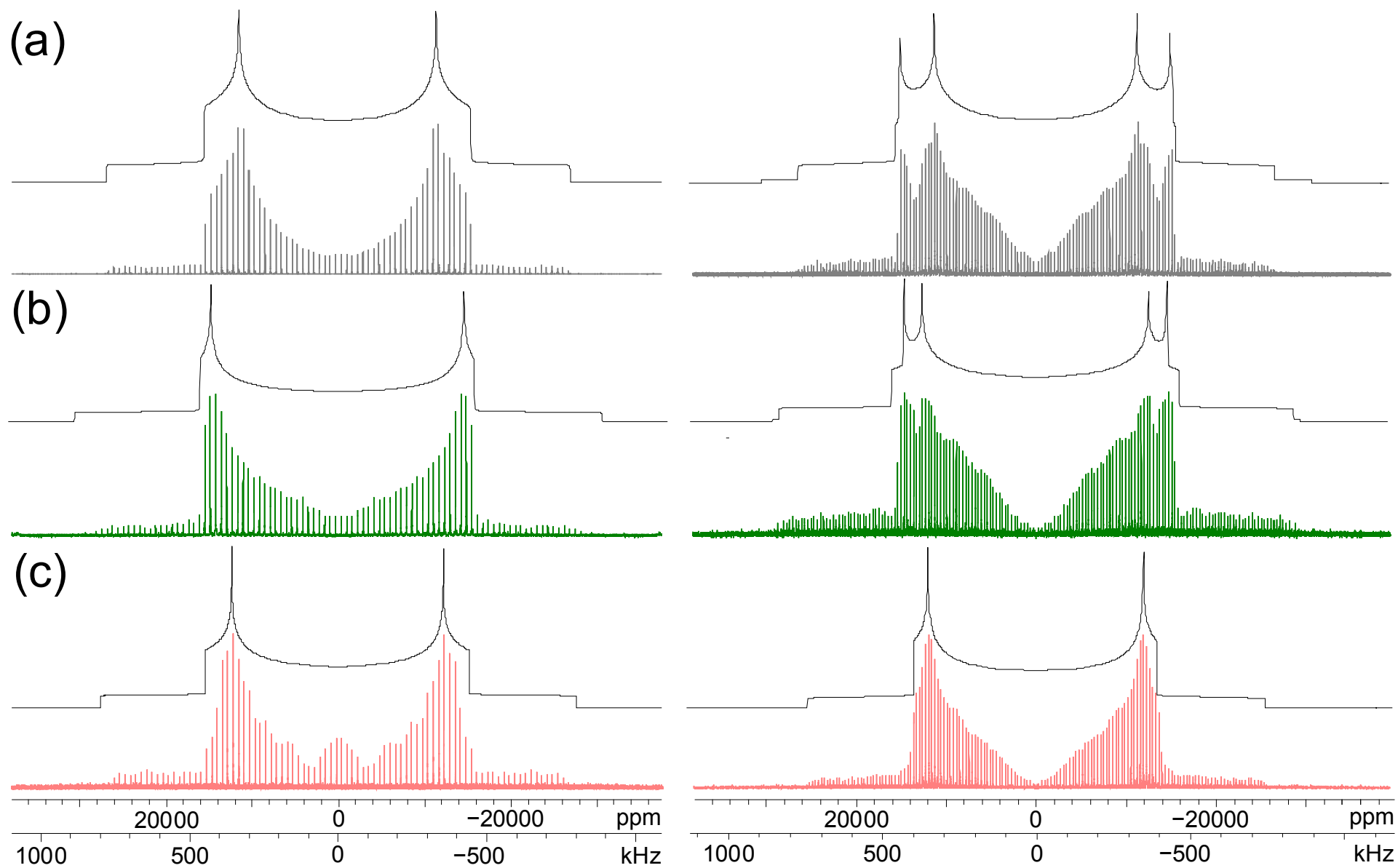


Figure 5. ^{14}N static NMR spectra (bottom traces) and simulations (top traces) of (a) $\text{Pt}(\text{NH}_3)_4\text{Cl}_2 \cdot \text{H}_2\text{O}$, (b) MGS, and (c) MPS. Spectra on the left were acquired with direct-excitation WURST-QCPMG experiments, spectra on the right were acquired using ^1H - ^{14}N BRAIN-CP/WCPMG experiments.

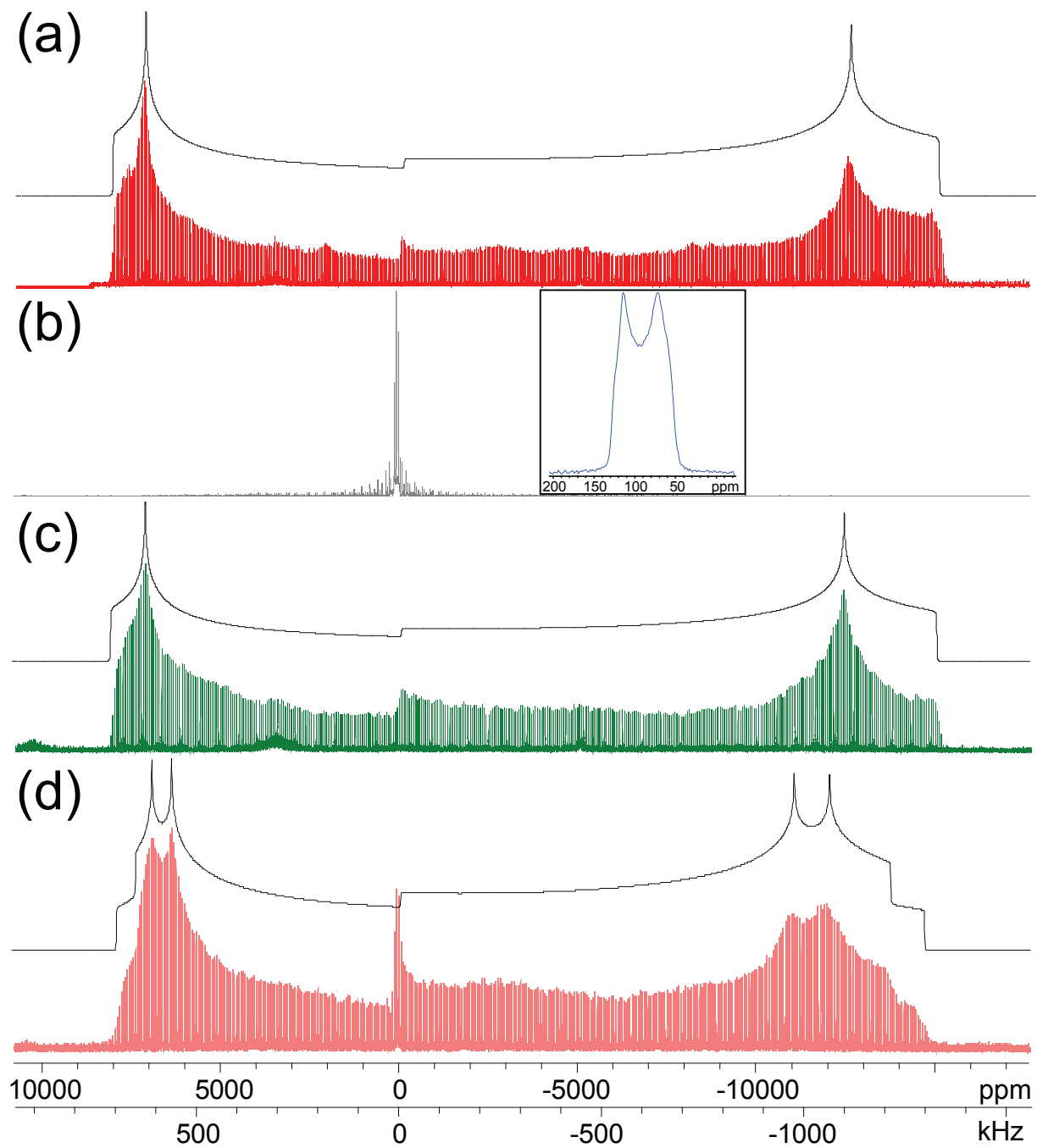


Figure 6. Static WURST-CPMG ^{35}Cl NMR spectra acquired at 21.1 T (bottom traces) and simulations (top traces) of (a) K_2PtCl_4 , (b) $\text{Pt}(\text{NH}_3)_4\text{Cl}_2 \cdot \text{H}_2\text{O}$ (with Hahn-echo experiment inset), (c) MGS, and (d) MPS.

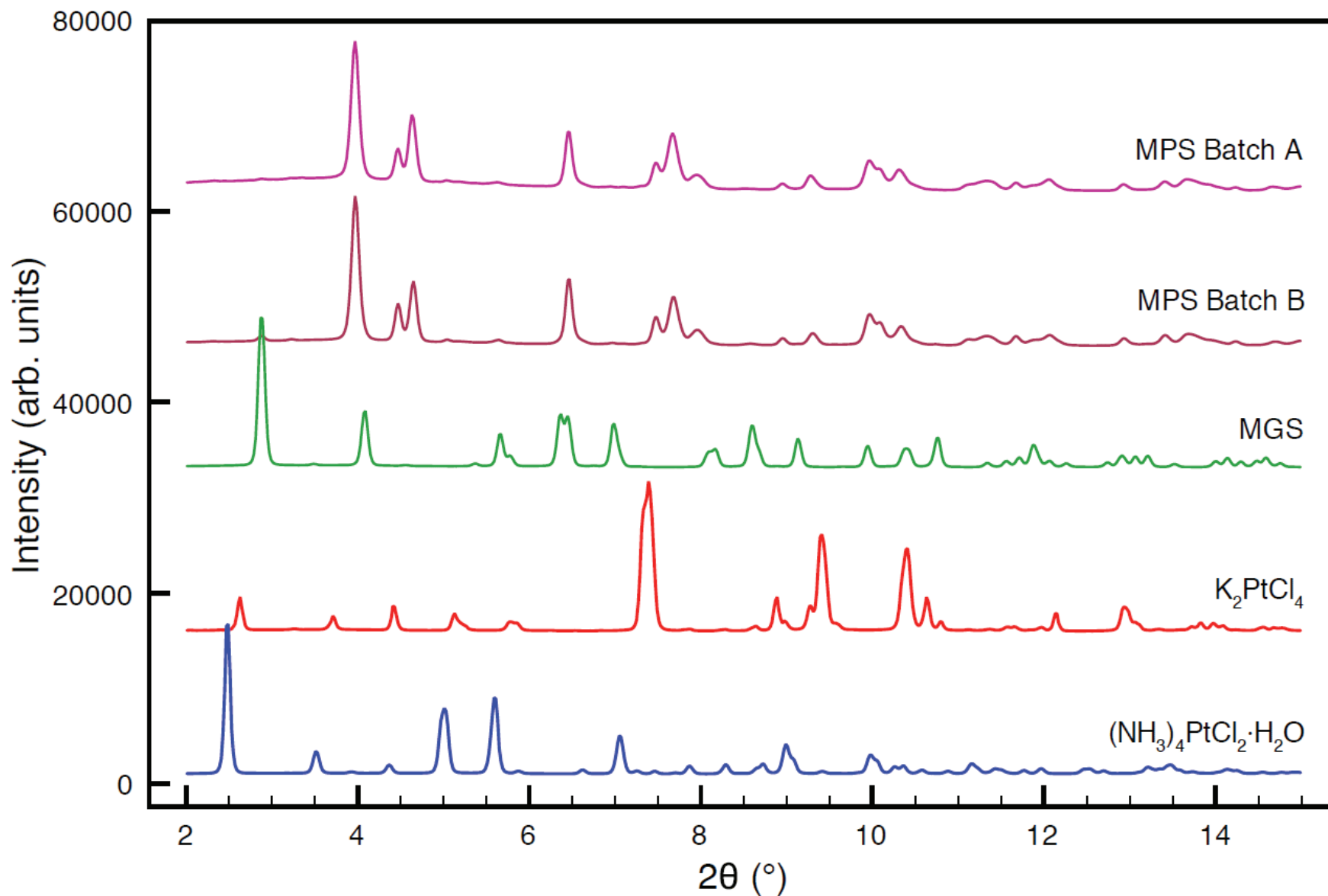


Figure 7. Powder X-ray diffraction patterns of square-planar Pt complexes. Two separate batches of MPS product were studied in order to assess the reliability of the synthesis.

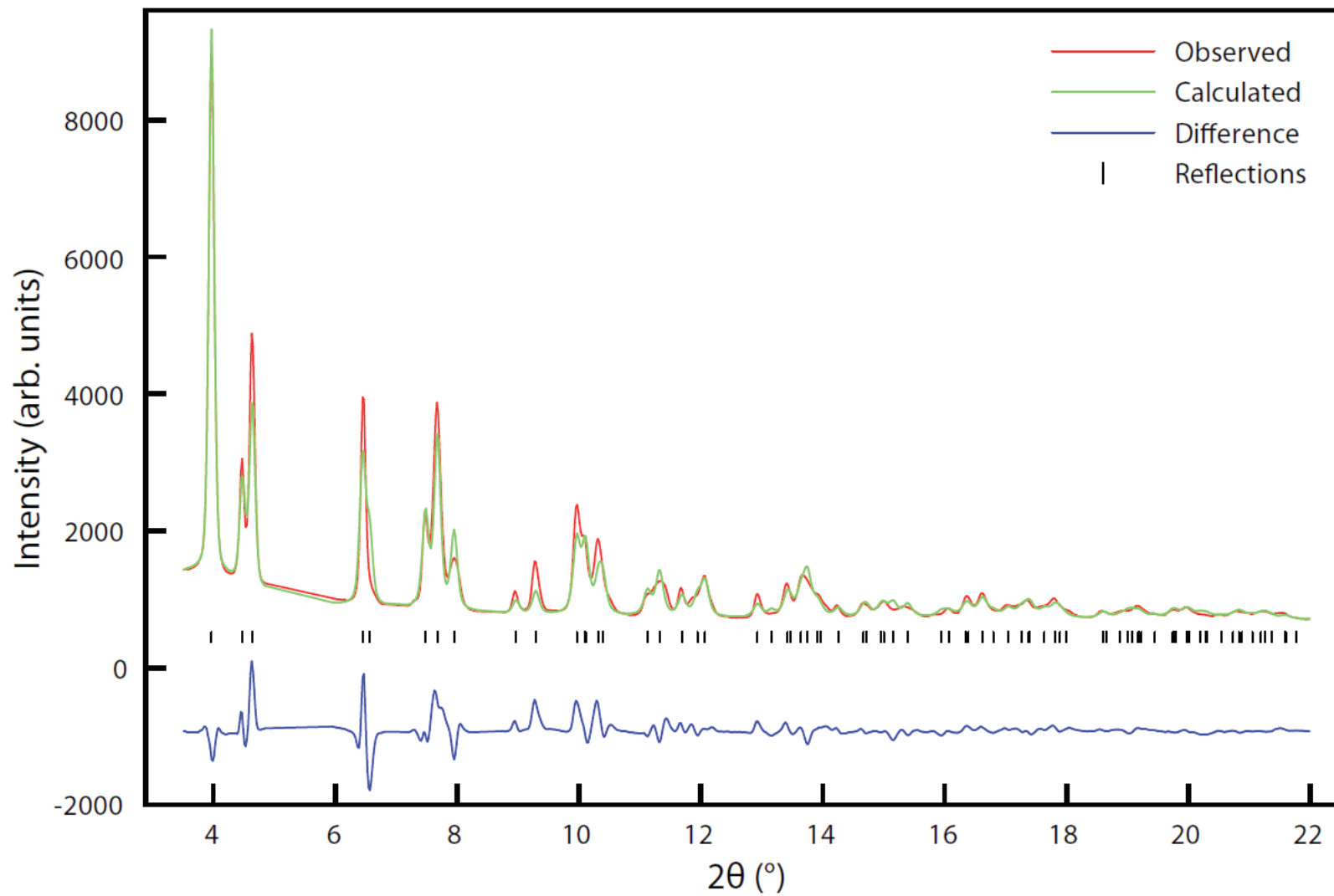


Figure 8. Leball fit for pXRD data of MPS using the parameters described in Table 4.

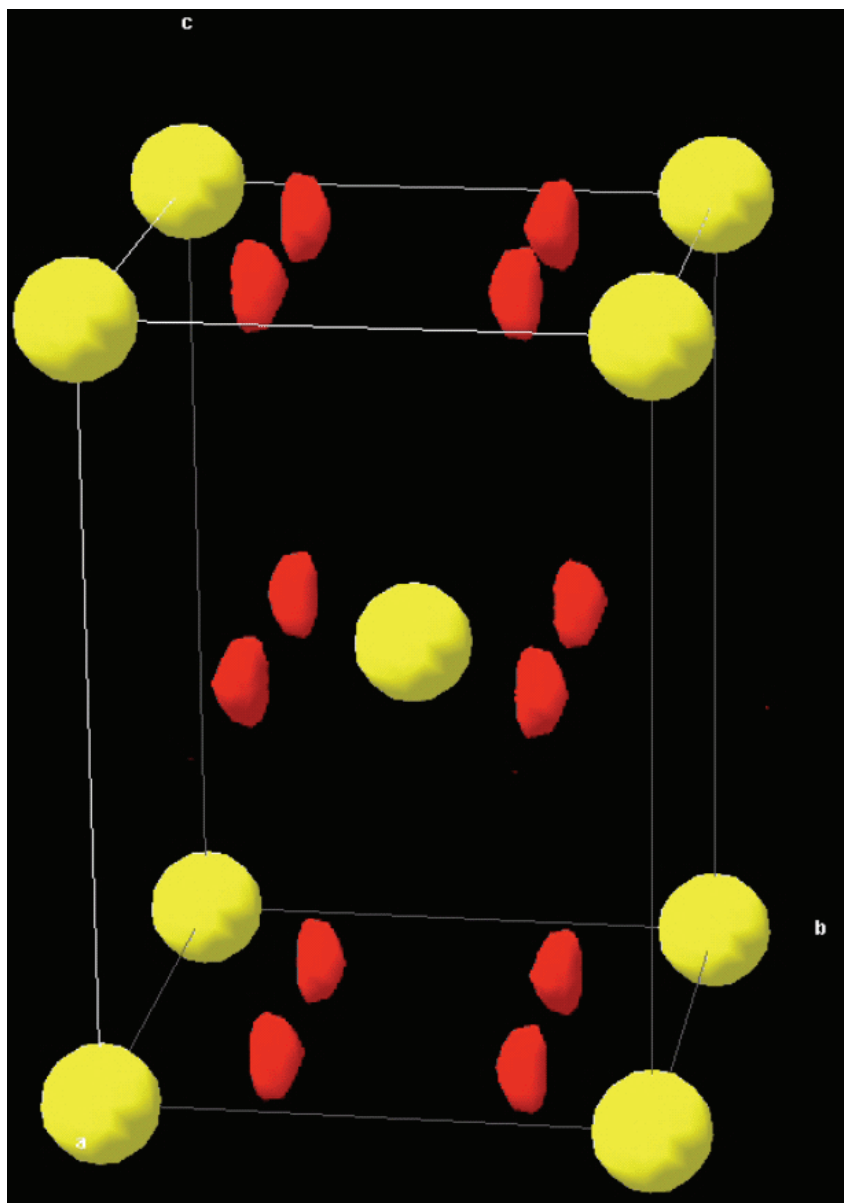


Figure 9. Visualization of the electron density map obtained via the refinement of MPS powder X-ray diffraction data. Yellow denotes Pt atoms, red denotes localized areas of electron density associated with Pt ligands.

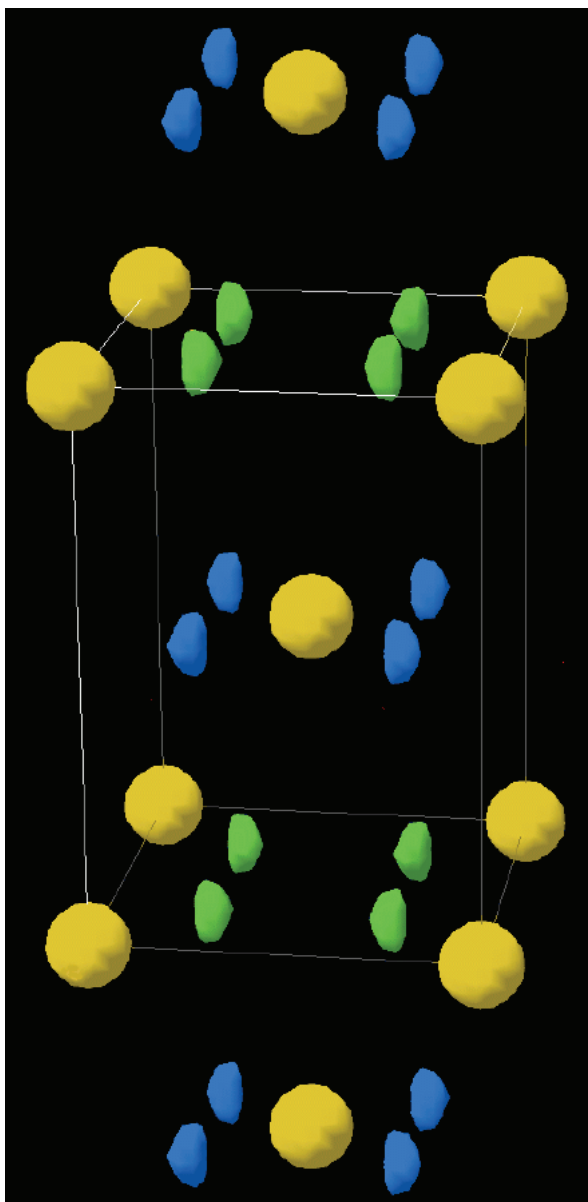


Figure 10. Proposed structural model of MPS, based on SSNMR and pXRD data. Yellow denotes Pt atoms, blue denotes electron density assigned to -NH_3 ligands, and green denotes electron density assigned to -Cl ligands.

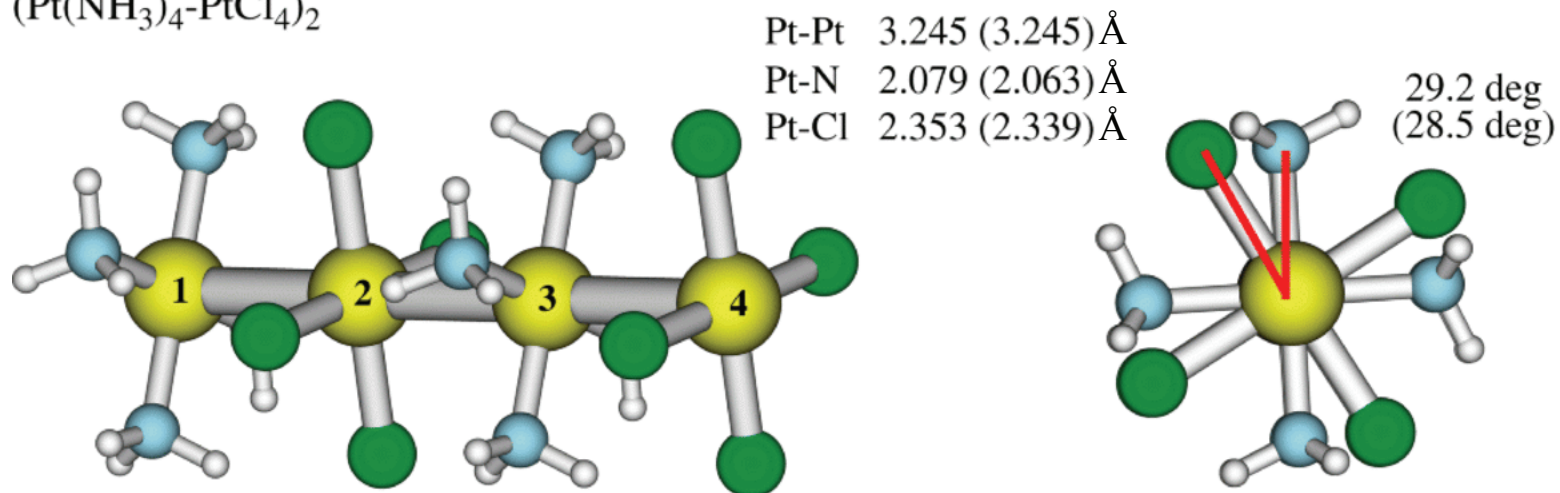
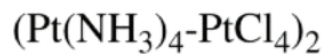
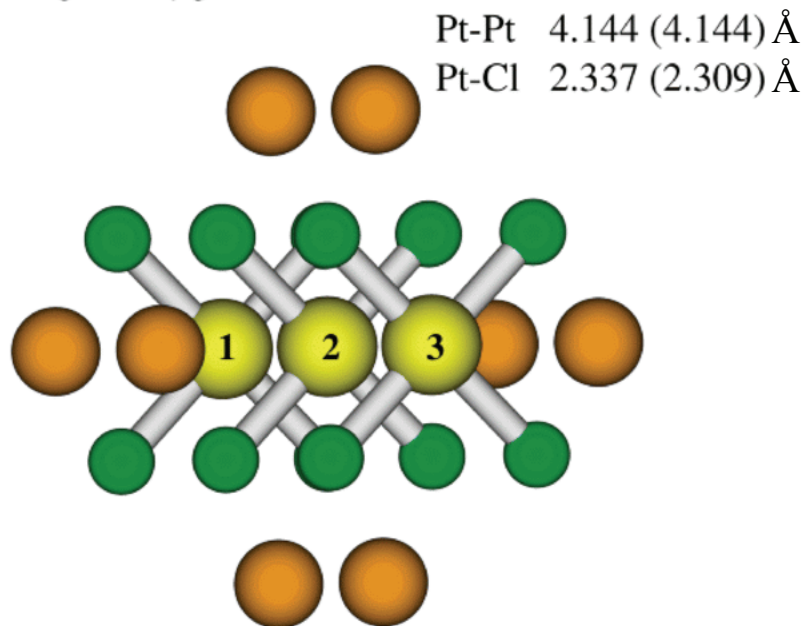
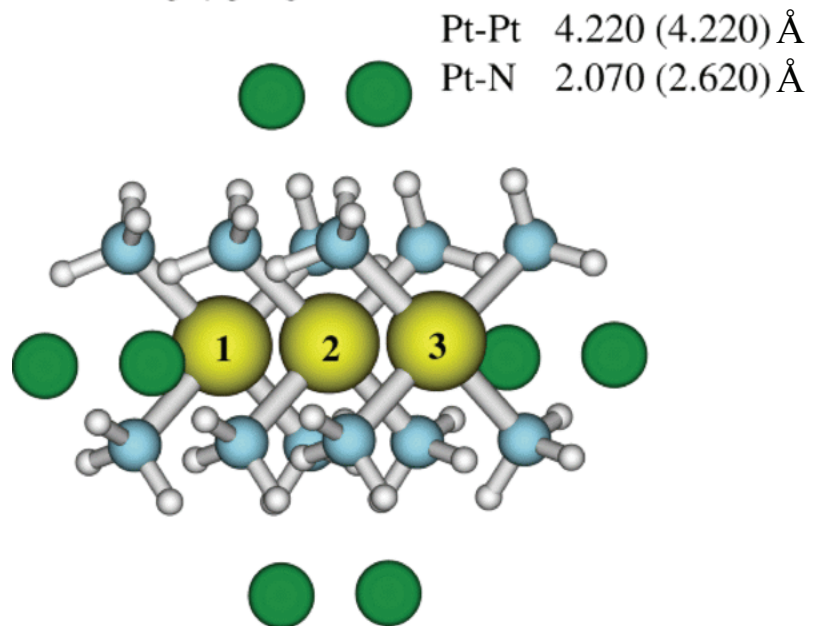
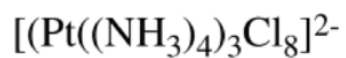
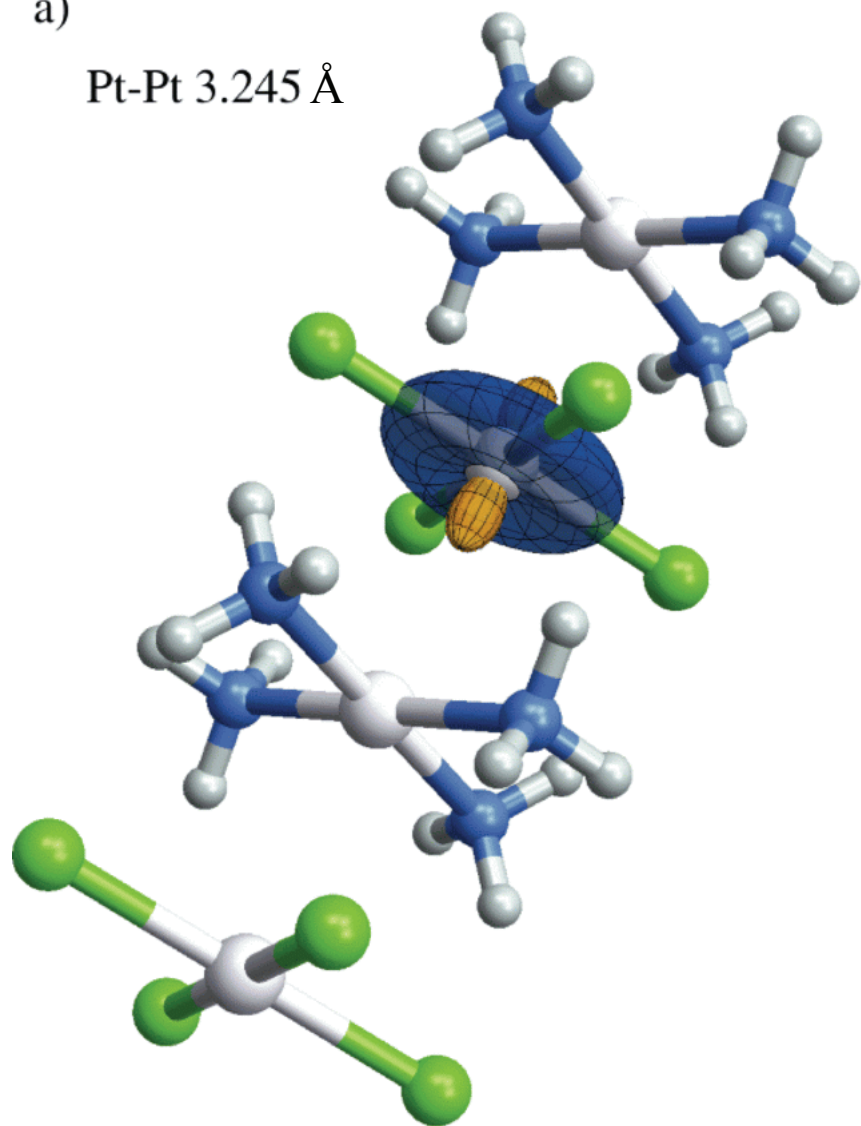


Figure 11. Molecular clusters used in the NMR calculations. The numbers listed correspond to calculated (experimental) geometric parameters.

a)

Pt-Pt 3.245 Å



b)

Pt-Pt 4.144 Å

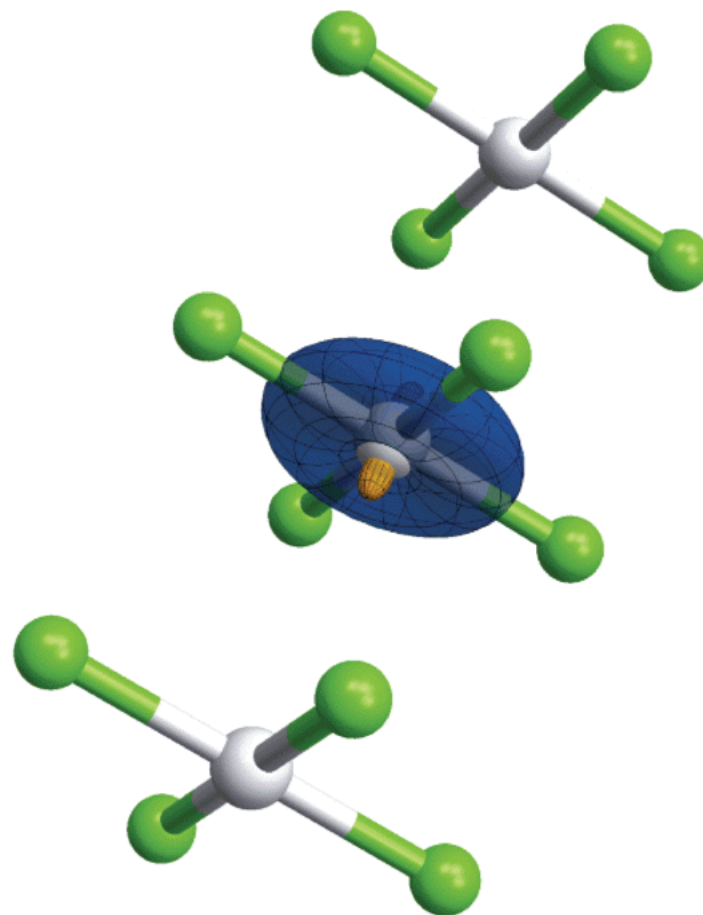


Figure 12. Graphical representations of the direction-dependent platinum shielding in (a) MGS and (b) K_2PtCl_4 . Blue and orange indicate positive and negative shielding, respectively. Polar plots of the shielding tensors are scaled by 0.025 pm/ppm.

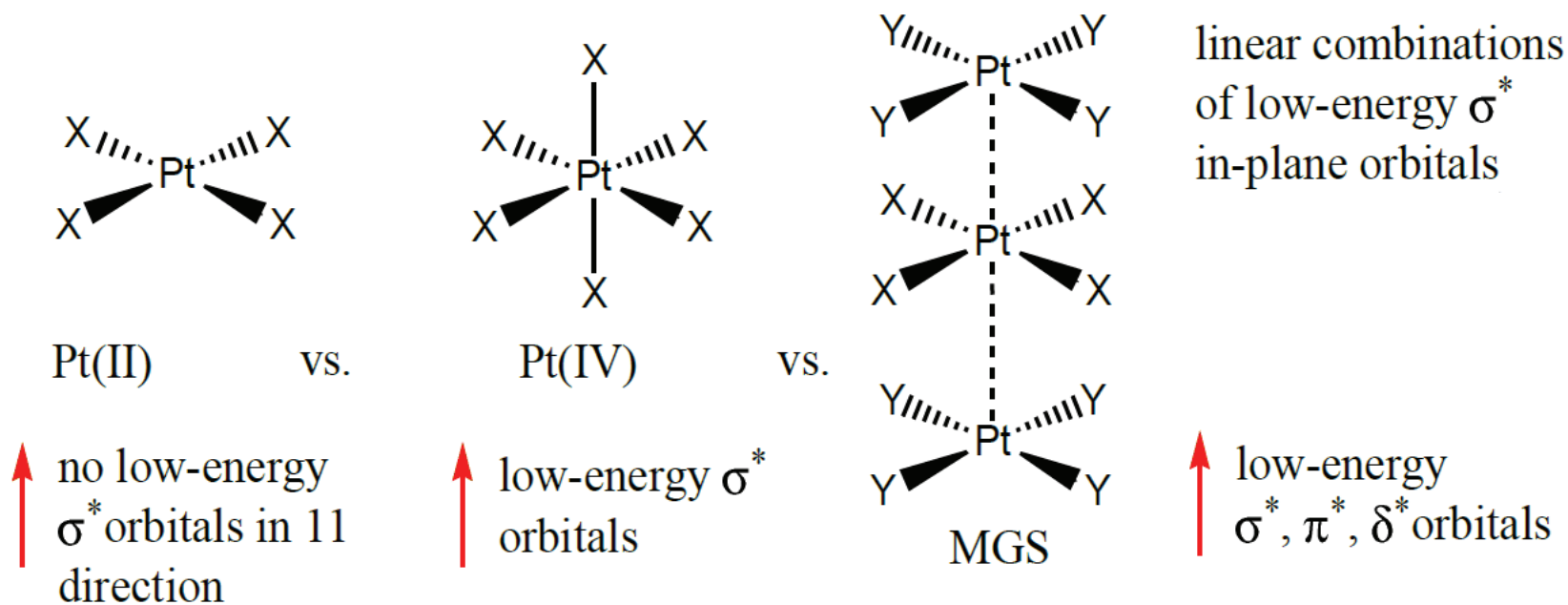


Figure 13. If low-energy unoccupied orbitals can overlap with a 'magnetic field rotated' Pt 5d orbital, a deshielding contribution is obtained in the MS tensor component parallel to the field. This causes deshielding in 6-coordinate Pt(IV) vs. 4-coordinate Pt(II), as shown in Reference 68. In MGS, similar orbital interactions create deshielding contributions from the Pt 5d nonbonding orbitals in all principal MS tensor components relative to the 4-coordinate Pt(II) starting reagents.